

YSO Jets Driven by Magnetic Pressure Generated through Stellar Magnetosphere–Disk Interaction

YISHENG TU,^{1,2} ZHI-YUN LI,^{1,2} ZHAOHUAN ZHU,^{3,4} XIAO HU,^{1,5} AND CHUN-YEN HSU^{1,2}

¹*Astronomy Department, University of Virginia, Charlottesville, VA 22904, USA*

²*Virginia Institute of Theoretical Astronomy, University of Virginia, Charlottesville, VA 22904, USA*

³*Department of Physics and Astronomy, University of Nevada, Las Vegas, NV, 89154-4002, USA*

⁴*Nevada Center for Astrophysics, University of Nevada, Las Vegas, 4505 S. Maryland Pkwy, Las Vegas, NV, 89154, USA*

⁵*Department of Astronomy, University of Florida, Gainesville, FL 32608, USA*

ABSTRACT

The origin of jets in young stellar objects (YSOs) remains a subject of active investigation. We present a 3D non-ideal magnetohydrodynamic simulation of jet launching in YSOs, focusing on the interaction between the stellar magnetosphere and the circumstellar disk. At the beginning of the simulation, the magnetosphere partially opens, forming two oppositely directed magnetic field regions: one threading the star and the other threading the inner disk. The latter dominates over the original disk field at small radii and contributes to launching a disk wind. In our model, the jet is launched from the interface between these regions by toroidal magnetic pressure generated along “two-legged” field lines, anchored at a magnetically dominated stellar footpoint and a mass-dominated point on the disk surface. Outflows are driven along these lines via a “load-fire-reload” cycle: in the “load” stage, differential rotation between the stellar and disk footpoints generates a toroidal magnetic field; in the “fire” stage, vertical gradients in toroidal field strength drive the outflow and release magnetic energy; and in the “reload” stage, magnetic reconnection between oppositely directed field lines resets the configuration, enabling the cycle to repeat. This process occurs rapidly and asynchronously across azimuthal angles, producing a continuous, large-scale outflow. From an energetic perspective, Poynting flux transports the toroidal field from the vicinity of the star into the polar cavity, powering the jet. Comparison with a disk-only model shows that the rotating stellar magnetosphere promotes bipolar jet launching by shaping a magnetic field geometry favorable to symmetric outflows.

Keywords: Young Stellar Objects (1834) — Circumstellar disks (235) — Jets (870) — Magnetohydrodynamics (1964) — Magnetic fields (994) — Stellar magnetospheres (1610)

1. INTRODUCTION

Star formation is often viewed as a collapse process, where a dense core, typically several to tens of thousands of AUs in size, collapses to form a young stellar object (YSO) consisting of a central star, a circumstellar disk, and, ultimately, planets. However, the reverse process, outflow, is also a fundamental aspect of the formation and evolution of YSOs. Outflows play a crucial role in shaping the chemical and dust distribution within individual star-forming systems (Y. Tsukamoto et al. 2021; L. Cacciapuoti et al. 2024; A. Morbidelli et al. 2024) and influence the formation of nearby stars and planets by regulating the dynamics of molecular clouds (P. André

et al. 2014; D. Guszejnov et al. 2021; C.-H. Hsieh et al. 2023).

The most energetic component of the outflow is the jet, a highly collimated stream of gas traveling at speeds exceeding 10^7 cm s⁻¹, often extending thousands of AU or more in length (L. Podio et al. 2015; T. Ray & J. Ferreira 2021). Recent observations have provided greater insight into the structure of jets and their surrounding environments (e.g., C. Codella et al. 2014; A. de Valon et al. 2020; C.-F. Lee et al. 2021; E. T. Whelan et al. 2024; K. D. Assani et al. 2024; J. A. López-Vázquez et al. 2024; S.-Y. Hsu et al. 2024; V. Delabrosse et al. 2024). Accompanying the jet is a slower, more massive outflow known as the disk wind, which typically surrounds the jet with a wider opening angle (B. Tabone et al. 2017; I. Pascucci et al. 2023). Since both the jet and disk wind significantly impact both local and global star forma-

tion processes, understanding their driving mechanisms is crucial to understanding star formation. A key open question is whether the jet and disk wind share a common driving mechanism, particularly what powers the jet itself.

It is becoming a consensus that the jets and outflows are most likely magnetically driven. One commonly used model is the class of magnetocentrifugal models (F. H. Shu et al. 1995; R. Krasnopolsky et al. 1999; G. V. Ustyugova et al. 1999; R. Krasnopolsky et al. 2003; J. M. Anderson et al. 2005, 2006; X.-N. Bai & J. M. Stone 2013), where the centrifugal force launches outflows as a result of angular momentum transportation along a magnetic field line. While the magnetocentrifugal model and its variants, including the “disk wind” (R. D. Blandford & D. G. Payne 1982; R. E. Pudritz & C. A. Norman 1983) and “X-wind” (F. Shu et al. 1994; F. H. Shu et al. 2000; H. Shang et al. 2002; M. J. Cai et al. 2008) models, can effectively explain the excessive angular momentum carried by the jet, how the exact launching conditions can be met under observational and theoretical constraints remains unclear (S. J. Desch et al. 2010; P. Bjerkeli et al. 2016).

Another class of models is the Poynting flux-driven jet model, where the outflow is launched by a predominantly toroidal magnetic field that transfers energy and angular momentum to the gas (K. Shibata & Y. Uchida 1986; R. V. E. Lovelace et al. 2001; R. V. E. Lovelace & M. M. Romanova 2009; X. Guan et al. 2014). A related model is the “magnetic-tower” model (D. Lynden-Bell 1996; D. Lynden-Bell 2003; Y. Kato et al. 2004; M. Nakamura et al. 2007), where the loop-like toroidal magnetic fields stack on top of each other, forming a magnetic loop tower. This class of models is usually more mass-loaded than the magneto-centrifugal model, resulting in a more gradual acceleration. Although this class of models provides an alternative method of acceleration, the stability of the required magnetic condition and the necessary external pressure to collimate the jet pose challenges to this model (R. Moll et al. 2008; M. Huarte-Espinosa et al. 2012).

Either launching mechanism relies on energy and angular momentum extraction from its base, which is typically believed to be rooted in the inner disk or the star. One possibility is that the jet is driven by the disk alone. Since the YSO disk is expected to be magnetized, particularly during the early phase of disk evolution (J. Wurster & Z.-Y. Li 2018; W. H. T. Vlemmings et al. 2019; M. Galametz et al. 2020; B. Lankhaar et al. 2022; H.-W. Yen et al. 2024; Y. Tu et al. 2024; S. Ohashi et al. 2025), the magnetic field in the disk could channel the disk’s rotational energy and momentum to a large dis-

tance, forming a jet. Previous studies have investigated this possibility (e.g. F. Casse & R. Keppens 2002; S. X. Kato et al. 2002; J. M. Anderson et al. 2006; P. Tzeferacos et al. 2009; C. Fendt et al. 2011; C. Fendt & S. Sheikhnezami 2013; D. Stepanovs & C. Fendt 2016; W. Béthune et al. 2017; Z. Zhu & J. M. Stone 2018; J. P. Ramsey & D. A. Clarke 2019; G. Mattia & C. Fendt 2020a,b; B. Mishra et al. 2020; J. Jacquemin-Ide et al. 2021; T. Jannaud et al. 2023; D. Takaishi et al. 2024; Y. Tu et al. 2025b,a; S. Takasao et al. 2025), but the jet-launching problem remains. One possibility is a jet can be launched by the disk alone, the jet is typically weak and variable, sometimes prone to being unipolar. Thus, it is unclear how general this jet-launching mechanism is in explaining observed outflows.

One key ingredient missing in these disk-only jet models is the star, which can be connected to the inner disk through its magnetosphere. Observations have shown that YSOs could have a strong magnetosphere, and previous studies and simulations have primarily focused on how the magnetosphere influences the disk accreting onto the star (A. Bardou & J. Heyvaerts 1996; K. A. Miller & J. M. Stone 1997; M. M. Romanova et al. 2009, 2012; D. Lai 2014; S. Takasao et al. 2019; M. M. Romanova et al. 2021, 2025; Z. Zhu et al. 2024; Z. Zhu 2025). Outflow launching from the magnetosphere-disk boundary has been examined primarily in 2D (e.g., A. P. Goodson & R. M. Winglee 1999; M. M. Romanova et al. 2005; R. V. E. Lovelace et al. 2013; M. Čemeljić et al. 2013; R. V. E. Lovelace et al. 2014), and less in 3D (e.g., M. M. Romanova et al. 2009; S. Takasao et al. 2022; Z. Zhu 2025), showing the possibility of jet launching. Yet, how the magnetosphere participates in jet launching and how it interacts with the disk field remains uncertain. This paper focuses on modeling these key processes in a self-consistent 3D non-ideal magneto-hydrodynamic global model.

This study is an extension of Y. Tu et al. (2025b) and Y. Tu et al. (2025a), who studied outflow launching using the disk gas and disk magnetic field alone. Y. Tu et al. (2025b) performed a 2D axisymmetric model and identified a key ingredient in jet launching, the “avalanche accretion stream” along the disk surface, which actively provides the energy and momentum to the jet-launching gas. Y. Tu et al. (2025a) extended the models to 3D and identified a light-loaded magnetic-pressure-driven jet model in a disk-only case, whose jet is highly variable and asymmetric in both disk hemispheres. In this study, we follow the disk setup in Y. Tu et al. (2025a) and include the stellar magnetosphere to examine the effect of the magnetosphere on jet launching.

This paper is organized as follows. Sec. 2 describes the simulation setup and model parameters. Sec. 3 gives an overview of the simulation result and identifies the key components of the modeled jet-launching system. The jet-launching mechanism is described in detail in Sec. 4, followed by a discussion of this mechanism in the context of the star formation literature in Sec. 5. We conclude in Sec. 6.

2. METHOD

The following set of non-ideal MHD equations governs the evolution of the circumstellar disk threaded by open magnetic field lines with the inner disk truncated by the stellar magnetosphere:

$$\frac{\partial \rho}{\partial t} + \nabla \cdot (\rho \mathbf{v}) = 0, \quad (1)$$

$$\rho \frac{\partial \mathbf{v}}{\partial t} + \rho (\mathbf{v} \cdot \nabla) \mathbf{v} = -\nabla P + \frac{1}{c} \mathbf{J} \times \mathbf{B} - \rho \mathbf{g}, \quad (2)$$

$$\frac{\partial \mathbf{B}}{\partial t} = \nabla \times (\mathbf{v} \times \mathbf{B}) - \frac{4\pi}{c} \nabla \times [\eta_O (\mathbf{J} \times \hat{\mathbf{B}})], \quad (3)$$

where $\mathbf{J} = (c/4\pi) \nabla \times \mathbf{B}$ is the current density, and η_O the Ohmic Dissipation coefficient. Other symbols have their usual meanings.

We use the **Athena++** code (J. M. Stone et al. 2020) to solve the governing equations in Cartesian coordinates with static mesh refinement (SMR). The initial condition setup is similar to Y. Tu et al. (2025a), with the addition of the stellar magnetosphere. We refer the readers to Y. Tu et al. (2025a) for a detailed description of the hydro, ionization, and non-ideal MHD setup, which are briefly summarized here.

We adopt a power law $\rho = \rho_0 (r/r_0)^{-1.35}$ for the density of the disk midplane with $\rho_0 = 10^{-9} \text{ g cm}^{-3}$ and $r_0 = 6.3 \times 10^{-2} \text{ au}$ following Y. Tu et al. (2025b). To model the truncation of the disk due to the stellar magnetosphere, the midplane density decreases as

$$\rho(r < r_{\text{trun}}) = \rho \left(\frac{r}{r_{\text{trun}}} \right)^p, \quad (4)$$

where $r_{\text{trun}} = 0.1 \text{ au}$ and $p = -10$. The remainder of the density is prescribed by assuming the disk is in isothermal hydrostatic equilibrium. To minimize numerical problems and ensure runability, we implement a similar density floor as in Y. Tu et al. (2025b):

$$\rho_{\text{floor}}(r) = \begin{cases} \rho_f; & r < r_f, \\ \rho_f (r/r_f)^{q_f}; & \text{otherwise,} \end{cases} \quad (5)$$

where $\rho_f = 6 \times 10^{-12} \text{ g cm}^{-3}$, $r_f = 0.015 \text{ au}$. $q_f = -5$ allows a rapid drop in the density floor towards a large

radius where a density floor is unnecessary. To speed up the simulation during the later stages, we increase the density floor coefficient ρ_f to $2.4 \times 10^{-11} \text{ g cm}^{-3}$ after $t = 1.0 \text{ yr}$. The thermal and non-ideal MHD setup is identical to Y. Tu et al. (2025a), where thermal ionization of alkali metals keeps the inner disk ($r \lesssim 0.13 \text{ au}$, the active zone) and the envelope in the ideal MHD limit, and Ohmic dissipation dominates the outer disk ($r \gtrsim 0.13 \text{ au}$, the dead zone).

To quantify and trace the amount of mass introduced by the density floor, we utilize the “passive scalars” in **Athena++** to differentiate between the real gas in the simulation (defined as all the mass present in the active domain at initialization) and the added gas introduced by the density floor. The real gas dominates the outflow and outflow-launching region throughout the simulation. In contrast, the added mass primarily resides in the low-altitude infalling region around the polar axis (i.e., the polar region shown in Figure 5) and the inner magnetosphere, where the star rapidly accretes it.

Following Z. Zhu et al. (2024) and Z. Zhu (2025), we incorporate a dense “star” at the center of the simulation to minimize numerical diffusion of the stellar magnetosphere. This approach leverages the Cartesian coordinate system, which avoids the presence of voids within the simulation domain. The stellar radius is $R_\star = 0.015 \text{ au}$ (about $3.2 R_\odot$), with a central density of 1.4 g cm^{-3} . The remainder of the stellar density is calculated assuming the star is in isothermal hydrostatic equilibrium. To avoid numerical problems due to too large a density gradient at the stellar surface, we separate the star from the remainder of the simulation domain by setting a “fixing radius” $r_{\text{fix}} = 0.018 \text{ au}$, within which the hydro quantities are reset to their initial values at each time step, while the magnetic field remains untouched. The passive scalars are set to 0 within r_{fix} at every time step. The gas in r_{fix} is assumed to rotate as a solid body with a rotational period of 12 days (corresponding to the Keplerian rotation period at 0.1 au).

The gravitational force is modeled by assuming that stellar gravity dominates the gravitational acceleration everywhere in the simulation. The stellar gravity is modeled as a point-source gravity, with a smoothing towards $r = 0$ to avoid the singularity

$$a_g(r) = \begin{cases} 0; & r < r_s, \\ -\frac{GM_\star}{r^2} \frac{(r-r_s)^2}{(r-r_s)^2 + r_s^2} \hat{\mathbf{r}}; & \text{otherwise,} \end{cases} \quad (6)$$

where $r_s = 0.012 \text{ au}$.

To ensure divergence-free initial condition and model both the open magnetic field lines threading the disk and the stellar magnetosphere, the global vector potential is

the sum of the vector potential of the magnetosphere and the open disk field, i.e.

$$\mathbf{A} = \mathbf{A}_{\text{disk}} + \mathbf{A}_{\text{mag}}, \quad (7)$$

where \mathbf{A}_{disk} is the same as the vector potential used in Y. Tu et al. (2025a). The stellar magnetosphere is modeled following Z. Zhu et al. (2024), using a vector potential

$$\mathbf{A}_{\text{mag}} = \frac{\bar{\mathbf{m}} \times \mathbf{r}}{r_c^3}, \quad (8)$$

where $r_c = \max(r, r_s/2)$. $\bar{\mathbf{m}}$ is chosen to be in the $-\hat{z}$ direction and of such magnitude that the initial magnetic field strength at the surface of the star is about 2000 Gauss. This choice of $\bar{\mathbf{m}}$ ensures that the magnetic field of the magnetosphere points upward on the disk midplane, aligned with the direction of the initial open disk field.

The computation domain and mesh refinement are chosen to best resolve the disk and the outflow-launching polar region while keeping a reasonable computational cost. The simulation domain spans ± 10 au in the \hat{x} and \hat{y} directions, and ± 20 au in the \hat{z} direction. The root grid has a resolution of $64 \times 64 \times 128$, ensuring all cells are cubic. Nine levels of refinements are applied in the simulation, with the finest level applied in the disk (± 0.04 au in the \hat{x} and \hat{y} directions, and ± 0.02 au in the \hat{z} direction), and in the outflow region (± 0.02 au in the \hat{x} and \hat{y} directions, and ± 0.04 au in the \hat{z} direction). The remainder of the grid is generated automatically by applying the condition that adjacent meshblocks can only differ by at most 1 level of refinement. To reduce numerical diffusion within the star but not add too much computational cost, we apply two additional levels of refinement inside the star: level 10 covers ± 0.01 AU, and level 11 resolves the central ± 0.005 au. This refinement strategy keeps the stellar magnetosphere stable throughout the simulation. As a result of the mesh refinement, the finest cell size is $(0.0006 \text{ au})^3$ in the active domain, and $(0.00015 \text{ au})^3$ inside the star.

3. RESULT

In this section, we present an overview of our simulation results, highlighting key features of the jet structure. Figure 1 shows a 3D rendering of the jet in our model, where blue and red contours represent the outflow in the upper and lower hemispheres, respectively. Each hemisphere contains two layers: the outer layer encloses gas moving at speeds exceeding $\pm 100 \text{ km s}^{-1}$, while the inner layer highlights gas with speeds exceeding $\pm 200 \text{ km s}^{-1}$, illustrating the presence of a powerful bipolar jet. To avoid obscuring the jet, the disk is visualized as a toroidal structure around the midplane, with

most of its mass removed for clarity. The white lines represent magnetic fieldlines, and velocity streamlines are shown by the black lines.

The partial opening of the magnetosphere during the early stages of simulations involving a stellar dipole is a well-known process (e.g. A. P. Goodson & R. M. Winglee 1999; M. M. Romanova et al. 2009; P. S. Lii et al. 2014). In this phase, the initially closed outer dipole field lines that thread the disk inflate and eject poloidal magnetic loops. This magnetic ejection results in the partial opening of the magnetosphere as the system undergoes its initial adjustment.

The initial adjustment results in a characteristic magnetic field geometry. To illustrate the magnetic field geometry and its relationship with the outflow, we show in Figure 2 the magnetic fieldlines overplotted on the projected \hat{z} -direction velocity v_z^p , defined as

$$v_z^p = v_z \frac{z}{|z|}, \quad (9)$$

so outflow in both the upper and lower hemispheres is positive whereas inflow is negative. The magnetic field geometry can be crudely divided into four zones: the permanently closed stellar magnetosphere near the star (enclosed by the magenta line in Figure 2), the $-\hat{z}$ direction opened stellar field attached to the star (roughly enclosed by the cyan lines), the large-scale open $+\hat{z}$ -direction field (similar to the original disk field, the outer region marked by the green lines), and the less ordered field lines lying in between the former two (between the green and cyan lines). This overall magnetic field structure remains consistent throughout the simulation after the initial adjustment. Since the magnetic field configuration plays a crucial role in launching the outflow, we first examine its properties before discussing each outflow component in detail.

3.1. Magnetic flux evolution

To quantify the opening of the magnetosphere field during simulation, Figure 3 shows the downward magnetic flux ($-\hat{z}$ direction) at $z = \pm 5$ au as a function of time for the upper and lower hemispheres, respectively. Since the disk's magnetic field is oriented upward, any downward flux at these heights must originate from the opening of the stellar magnetosphere. For reference, Figure 3 also shows the total stellar magnetospheric flux, defined as the total downward magnetic flux at the midplane. Due to magnetic reconnection of the innermost magnetospheric loops inside the star, the total stellar magnetic flux decreases slightly at the beginning of the simulation before stabilizing at approximately $-8 \times 10^{26} \text{ G cm}^2$. The opened magnetospheric

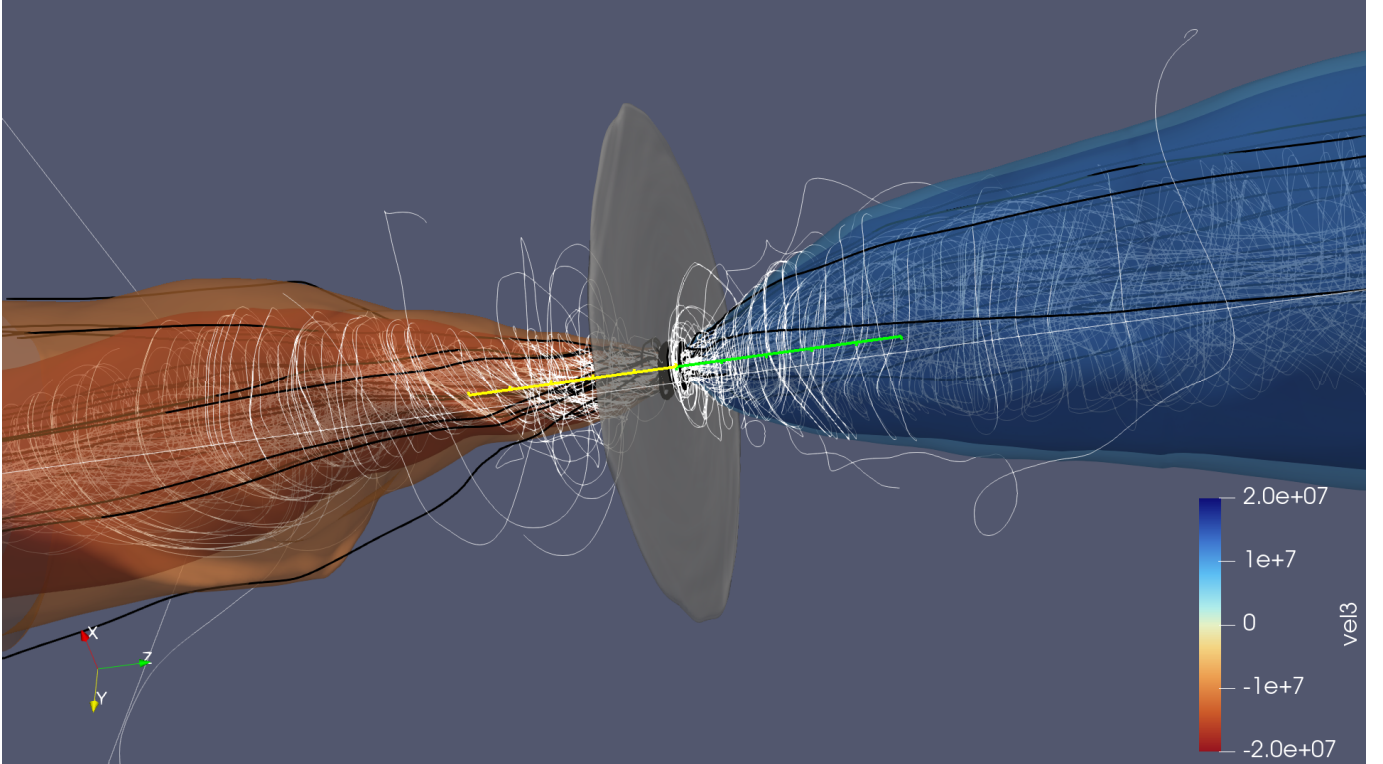


Figure 1. 3D rendition of the bipolar jet launched in our model. The outer red and blue shells are isosurface contours at 100 km s^{-1} , whereas the inner ones are at 200 km s^{-1} . The gray structure on the equatorial plane represents the disk. For reference, the green and yellow lines each have a length of 5 au, illustrating the physical scale of the system. An animated version of this figure can be found at: <https://figshare.com/s/67335cb1846eca1edcb1>. The movie is 27 seconds long, highlighting the strong bipolar outflow from the simulation’s beginning (0 yr) to the end (5.5 yr).

flux remains around $-8 \times 10^{25} \text{ G cm}^2$, accounting for about 10% of the total magnetospheric flux.

The opened magnetic flux dominates the magnetic field of the inner disk. It is equivalent to the total initial flux of the disk within $r \approx 7 \text{ au}$, and diffuses outward gradually. Figure 3 illustrates the evolution of the net magnetic flux enclosed within a given radius on the mid-plane over time. Due to the strong, negative magnetic field inside the star, the enclosed flux initially drops to a highly negative value at small radii, then gradually returns to positive as more upward-directed field lines are included. The zero-crossing point marking the approximate boundary between the original disk field and the stellar field slowly expands outward, reaching $\sim 1 \text{ au}$ by $t = 4.0 \text{ yr}$.

Although the newly opened field lines within 1 au originate from the stellar magnetosphere rather than the original disk field, they thread the disk vertically and link the dense midplane to the less dense surface layers, just as the original disk field. This connection facilitates the launching of a slower disk wind at larger cylindrical radii, which we examine in the following subsection.

3.2. Disk Wind from Opened Magnetospheric Field

The disk wind is a slower, high-density outflow at large cylindrical radius compared to the jet (see § 3.4 below). To illustrate the properties and launching mechanism of the disk wind, we show in Figure 4 the azimuthally averaged quantities in the disk wind region. Panels (a) and (b) show the density and the projected \hat{z} -direction velocity, respectively. Any outflow away from the disk mid-plane has a positive value. The disk wind has a density $\approx 10^{-13} \text{ g cm}^{-3}$ near the base (around $r \approx 0.5 \text{ au}$), and a density of $\approx 10^{-14} \text{ g cm}^{-3}$ at higher altitudes. The outflow velocity of the disk wind is around 10^6 cm s^{-1} , slower than the jet but still above the escape velocity at high altitudes.

Y. Tu et al. (2025a) identify two components for the disk wind: an MRI-active disk wind and a laminar disk wind. In their case, the inner disk wind is MRI-unstable, leading to a turbulent outflow, whereas the outer disk wind is MRI-stable, resulting in a laminar wind. The MRI stability is measured using the dimensionless parameter (Y. Tu et al. 2025a)

$$q \equiv \frac{\lambda}{H}, \quad (10)$$

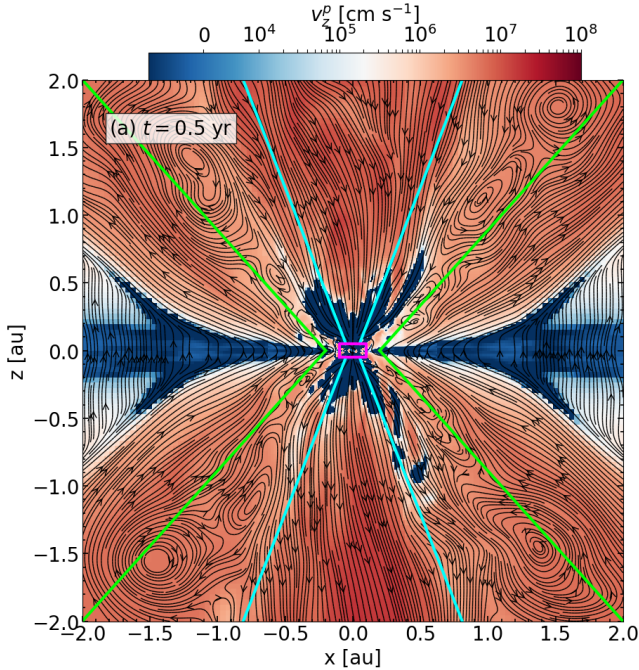


Figure 2. Magnetic field geometry, represented by the magnetic field lines on a meridional slice, after the initial adjustment in the simulation. The background color map shows the projected \hat{z} -direction velocity v_z^p (equ. 9). The magnetic field structure can be roughly divided into four distinct zones, delineated by the magenta, cyan, and green lines. The magenta line encloses the permanently closed stellar magnetosphere; the cyan line marks the boundary of opened stellar field lines that still thread the star; the green line outlines the extent of the large-scale magnetic field lines threading the disk. The region between the cyan and green lines corresponds to a reconnecting, outflow-driving zone where the interaction between stellar and disk fields powers the outflow.

where $H = R/10$ is the disk scale height and λ is the most unstable MRI wavelength given by (Z. Zhu & J. M. Stone 2018)

$$\lambda = 2\pi \sqrt{\frac{16}{15} \frac{v_A}{\Omega}}. \quad (11)$$

Here, v_A is the Alfvén speed and Ω is the local orbital frequency. Following Y. Tu et al. (2025a), we choose the range $0.1 < q < 10$ to denote where MRI is most efficient.

Figure 4(c) shows this q parameter, illustrating a zone between the jet and the disk wind in both hemispheres where q is within the optimal range. The disk wind can thus be divided into the MRI-active disk wind at a small cylindrical radius and the MRI-stable disk wind at a larger cylindrical radius, particularly along the upper hemisphere. However, similar to Y. Tu et al. (2025a), the MRI-active disk wind eventually merges with the laminar disk wind at high altitudes, where MRI can no

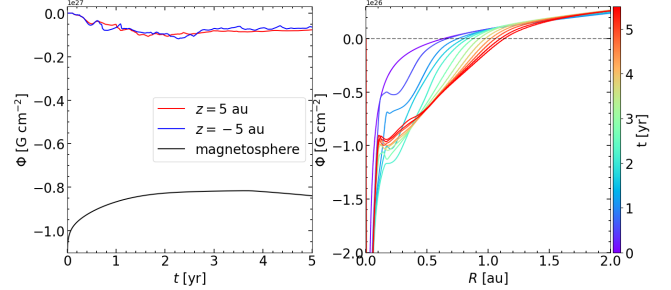


Figure 3. Magnetic flux evolution in the simulation. **The left panel** shows the total magnetospheric flux (black line), defined as the maximum magnitude of the total downward \hat{z} -directed magnetic flux integrated azimuthally at each cylindrical radius. The red and blue lines indicate the amount of opened stellar magnetosphere flux, measured as the maximum magnitude of azimuthally-integrated downward B_z at $z = \pm 5$ au above and below the disk midplane, respectively. **The right panel** shows the time evolution of the enclosed magnetic flux at each cylindrical radius at the midplane. The stellar magnetosphere primarily contributes to the negative flux at small radii, while the disk field dominates the positive flux at larger radii.

longer be sustained. As a result, at these altitudes, the primary distinction is between the jet and the disk wind.

To illustrate the kinematics of the disk wind, we show the plasma- β and the kinetic- β in Figure 4(d) and (e), respectively. They are defined as

$$\beta = \frac{P}{B^2/8\pi}, \quad (12)$$

$$\beta_K = \frac{\rho v^2/2}{B^2/8\pi}, \quad (13)$$

measuring the ratios between the thermal and ram pressures and the magnetic pressure. The plasma- $\beta < 1$ in the disk wind indicates that thermal energy is negligible compared to magnetic energy. Kinetic- $\beta > 1$ in the disk indicates that kinetic energy (primarily from rotation) dominates the magnetic energy.

The dominance of kinetic energy results in the centrifugal force outweighing the magnetic force in the cylindrical- \hat{R} direction. Figure 4(f) and (g) show the ratio between magnetic and centrifugal forces, and the magnitude of the magnetic force in the cylindrical- \hat{R} direction, respectively. The radial-direction magnetic force is given by

$$a_{B,R} = \left[\frac{1}{4\pi\rho} (\nabla \times \mathbf{B}) \times \mathbf{B} \right]_R, \quad (14)$$

and the centrifugal force is given by

$$a_{R,\text{cent}} = \frac{v_\phi^2}{R}. \quad (15)$$

While the magnetic force generally points in the $-\hat{R}$ direction (towards the axis), its magnitude is insufficient to counteract the outward centrifugal force. This imbalance leads to an increasing opening angle of the disk wind.

The magnetic force is primarily responsible for driving the outflow in the \hat{z} direction. Figure 4(h), (i), and (j) show the projected total magnetic force in the \hat{z} direction, the effective magnetic pressure component, and the effective magnetic tension component, respectively. The projected total magnetic force is given by

$$a_{B,z}^p = \frac{z}{|z|} \left[\frac{1}{4\pi\rho} (\nabla \times \mathbf{B}) \times \mathbf{B} \right]_z, \quad (16)$$

and following Y. Tu et al. (2025a), we define the projected effective magnetic pressure and tension forces in cylindrical coordinates by removing the $B_z \frac{dB_z}{dz}$ term that does not contribute to overall acceleration:

$$a_{z,\text{pres}}^{p,\text{eff}} \equiv -\frac{z}{|z|} \frac{1}{4\pi\rho} \left(\frac{\partial B_\phi}{\partial z} B_\phi + \frac{\partial B_R}{\partial z} B_R \right), \quad (17)$$

$$a_{z,\text{tens}}^{p,\text{eff}} = \frac{z}{|z|} \frac{1}{4\pi\rho} \left(\frac{\partial B_z}{\partial R} B_R + \frac{\partial B_z}{\partial \phi} B_\phi \right). \quad (18)$$

It is evident that magnetic pressure drives the disk wind outflow, not the magnetic tension force. This result is consistent with the geometric argument and conclusion in Y. Tu et al. (2025a) that only magnetic pressure can drive an outflow when open magnetic field lines thread the disk.

3.3. Opened Stellar Field

As discussed in Sec. 3.1, part of the stellar magnetospheric field opens up. Half of the opened field threads the disk and becomes a “disk field”; the other half remains attached to the star and becomes an opened stellar field.

To illustrate the geometry of the opened stellar magnetic field, Figure 5(a) presents a density slice through the meridional plane, overlaid with magnetic field lines. On the displayed scale, the magnetic field in the polar regions above and below the star points in the $-\hat{z}$ direction, opposite to the field threading the disk (e.g., Figure 4), as expected.

The properties of this downward magnetic field and the gas kinematics are shown in Figure 5(b) and (c), respectively. The magnetic field strength is particularly strong in the polar cavity, reaching approximately 20 Gauss at $z = \pm 0.1$ au. The gas in the polar cavity immediately above and below the stellar magnetosphere rapidly falls toward the star because of strong gravity and insufficient rotational support. Given the low density and strong magnetic field in this region, it is unsurprising that the polar cavity is entirely magnetically

dominated, with plasma- β and kinetic- β values much lower than 1 (Figure 5[d] and [e]).

Although the majority of the open stellar field does not directly contribute to jet launching, it serves as a structural backbone for the jet in the magnetically dominated region. As we demonstrate in Section 3.4, the jet is primarily driven by toroidal magnetic pressure. However, a magnetic tower consisting predominantly of toroidal loops is inherently susceptible to kink instabilities (R. Moll et al. 2008; M. Huarte-Espinosa et al. 2012). The strong open stellar magnetic field in the polar region, which accounts for most of the open stellar flux, helps stabilize the jet by threading these loops along the polar axis, mitigating instabilities.

3.4. Magnetospheric jet

The jet is launched from the interaction between the star, its magnetosphere, and the surrounding disk, and propagates in the low-density polar cavity. Figure 6 outlines the jet’s location and key characteristics. At lower altitudes ($\lesssim 0.5$ au), the jet is confined between the opened stellar field near the polar axis (approximately delineated by the magenta line) and the disk wind/atmosphere at larger cylindrical radii (indicated by the green dashed line). At higher altitudes, the jet expands to fill the polar cavity, as shown in Figure 4[b].

To assess the relative contributions of various energy components in the jet-launching region—namely, gas thermal energy, gas kinetic energy, and magnetic energy—we examine the plasma- β and kinetic- β in Figure 6(c) and (d). As expected, the plasma- β remains well below unity throughout the jet region, except in the disk midplane, indicating that magnetic energy dominates over thermal energy. The kinetic- β is also less than 1 inside the jet-launching polar cavity, but rises above 1 just outside the jet boundary. This transition is a key feature in the launching process and is analyzed in more detail in Section 4.

Since both plasma- β and kinetic- β are below order unity in the jet-launching polar cavity, we focus on the magnetic forces to establish a foundation for our detailed examination of the jet-launching mechanism in section 4. The lower panels of Figure 6 illustrate the magnetic forces in the jet region. Figure 6[e] shows the total magnetic force, revealing that the acceleration of the outflow occurs primarily along the surface of the vertically extended disk, which also marks the boundary of the jet-launching cavity. Above approximately 1 au in both hemispheres, acceleration becomes less coherent (with alternating regions of acceleration and deceleration), indicating that the bulk of the flow acceleration has largely completed beyond this altitude. This is confirmed by

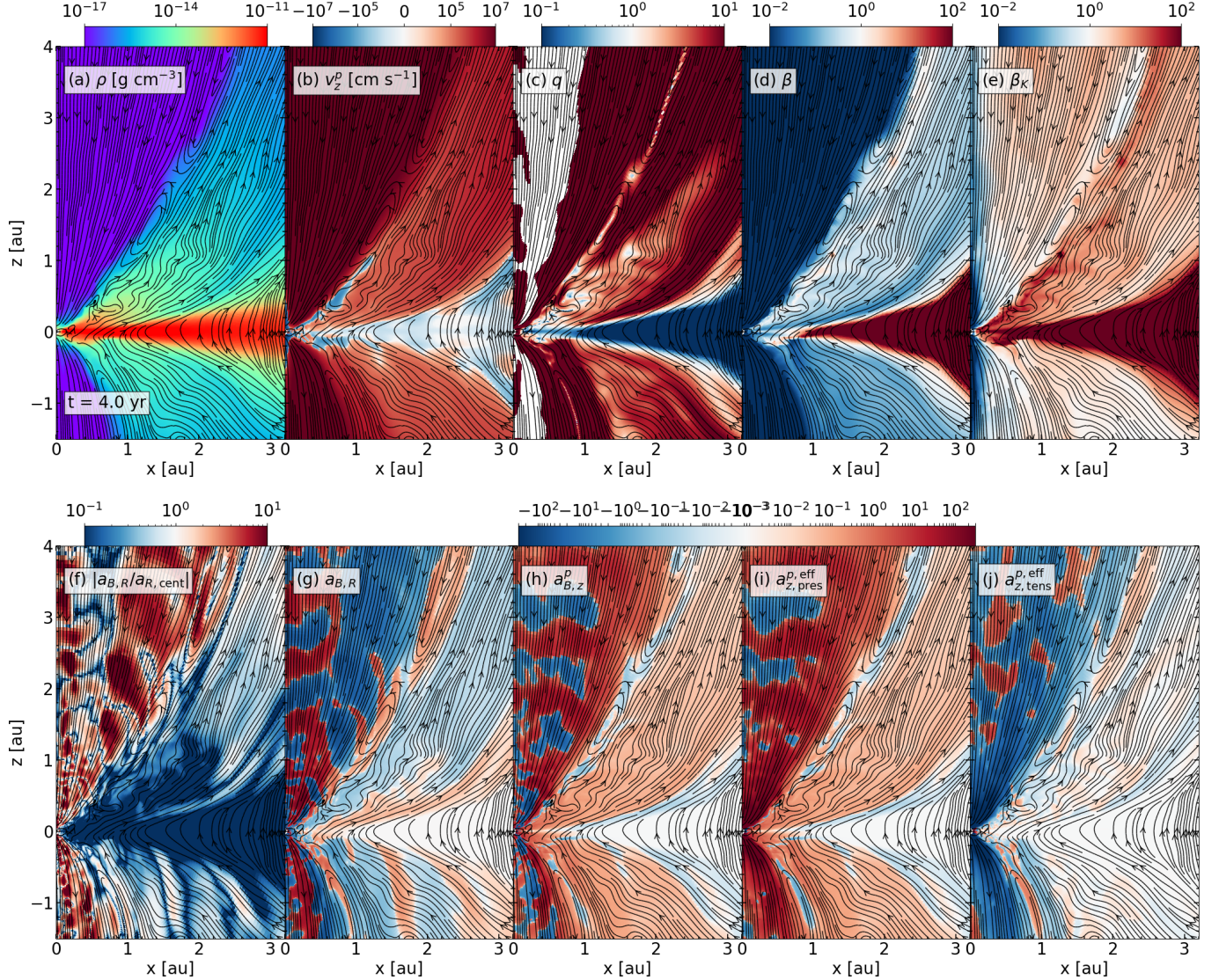


Figure 4. Overview of the outflow, particularly the disk wind at a large cylindrical radius surrounding the jet. **Panel (a) and (b)** show the density and projected \hat{z} -direction velocity (v_z^p , equ. 9) respectively; **panel (c)** shows the normalized MRI-turbulence wavelength (equ. 10; **panel (d) and (e)** show the plasma- β and (equ. 12) kinetic- β (equ. 13) respectively. The lower panels compare different force components in the disk wind. **Panel (f)** shows the ratio between the cylindrical- \hat{R} direction magnetic force and centrifugal force. **Panel (g), (h), (i), and (j)** show the magnitude of the gas acceleration in cylindrical- \hat{R} direction, total magnetic acceleration due to magnetic forces. The quantities are total gas acceleration in cylindrical- \hat{R} direction, the effective magnetic pressure component (equ. 17), and the effective magnetic tension component (equ. 18) respectively. These disk wind properties and forces show that the disk wind in this model is very similar to the disk wind in [Y. Tu et al. \(2025a\)](#).

velocities in the \hat{z} direction reaching several 10^7 cm s $^{-1}$ below 1 au, with minimal subsequent increase in velocity above this height.

As demonstrated in [Y. Tu et al. \(2025a\)](#), in systems with ordered, large-scale magnetic fields threading the disk, only magnetic pressure forces, not magnetic tension forces, can launch outflows in global models. Our simulations confirm this finding. Figure 6(f) and (g) display the effective magnetic tension acceleration (equ. 18) and effective magnetic pressure acceleration (equ. 17),

respectively. Magnetic tension acceleration generally points toward the midplane, while magnetic pressure acceleration points away from it. More specifically, Figure 6(h) shows the acceleration due to toroidal magnetic pressure gradient, defined as

$$a_{z,pres}^{p,tor} = -\frac{z}{|z|} \frac{1}{4\pi\rho} \frac{dB_\phi}{dz} B_\phi. \quad (19)$$

The toroidal magnetic pressure accounts for most of the magnetic pressure-driven jet acceleration. In the

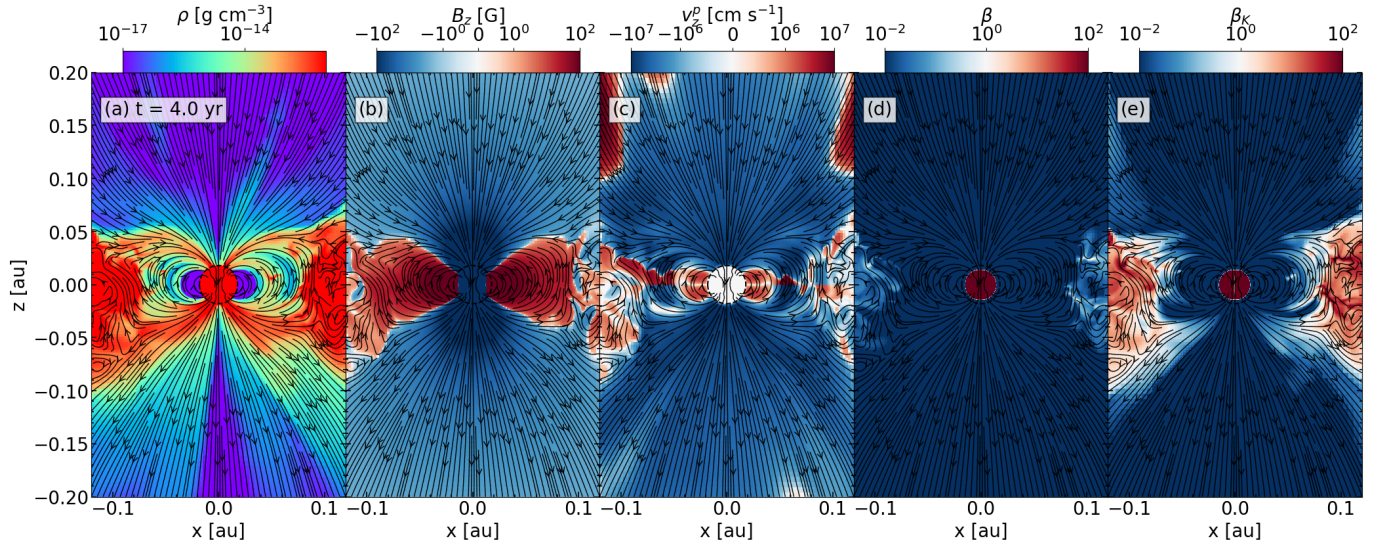


Figure 5. A zoom-in view focusing on the permanently closed stellar magnetosphere (around the midplane) and the opened stellar magnetic field threading the star (in the polar region above and below the star). **Panel (a)** shows the real density traced by the “passive scalars”, highlighting the magnetospheric accretion streams. The sphere in the middle is the inner boundary r_{fix} , where a star resides (see sec. 2 for a more detailed description of the setup). **Panels (b) and (c)** show the B_z field strength and v_z^p (equ. 9) respectively, illustrating the magnetic and dynamical properties of the region close to the star. **Panels (d) and (e)** show the plasma- β (equ. 12) and kinetic- β (equ. 13) respectively, indicating the magnetosphere and the polar cavity are both magnetically dominated.

following section, we will examine the mechanism generating this crucial toroidal magnetic field (Section 4).

4. JET LAUNCHING MECHANISM: “LOAD-FIRE-RELOAD”

This section presents a detailed description and analysis of the jet-launching mechanism in our model. The jet is launched through a cyclic process comprising three distinct phases: load, fire, and reload. Each phase corresponds to characteristic changes in the magnetic field configuration and dynamics. In the following subsections, we describe each step in detail and analyze how they collectively drive the jet-launching behavior observed in the simulation.

4.1. Load: charging B_ϕ by star-disk differential rotation

To illustrate the jet-launching mechanism, we zoom in on the inner part of the simulation in Figure 7, which shows the azimuthally averaged gas and magnetic field properties. Panels (a), (b), and (c) show the density, projected \hat{z} -direction velocity v_z^p , and kinetic- β , respectively. The jet resides in the low-density polar cavity, where $\rho \lesssim 10^{-14}$ g cm $^{-3}$, $v_z^p > 10^7$ cm s $^{-1}$ and $\beta_K < 1$. The low β_K highlights the magnetic dominance in the jet-launching polar cavity. A black dashed contour traces $\beta_K = 1$, the rough boundary between the high-density disk wind/atmosphere and the low-density jet.

On the scale shown in Figure 6, the jet is driven by magnetic pressure force primarily along the polar cavity-disk boundary, with a strong toroidal magnetic field. Since a toroidal field can in principle be generated wherever there is differential rotation along a field line, the most preferred field lines for toroidal field generation are those threading both the star, where the magnetically-dominated segment of the field line rooted on the star surface co-rotates with the star, and the disk, where the gas dominates and the field lines are forced to move with the gas at the local Keplerian velocity. We will first focus on these field lines, followed by a generalization to all field lines that experience field-gas differential rotation.

The field lines threading both the star and the dense disk generate a toroidal field in situ by a change in the angular speed of the rotation along the field line, as shown in Figure 7(d), which presents the ratio between the local angular velocity Ω and the Keplerian angular velocity Ω_K . Across the $\beta_K = 1$ boundary, the angular velocity transitions from nearly Keplerian in the disk to super-Keplerian above the disk. It is indicative of the differential rotation along the field line that leads to the toroidal field generation through field line twisting.

To showcase a magnetic field participating in this process, Figure 7 shows a 2D projection of a 3D field line, highlighted in solid magenta. One end of this field line is anchored on the star, which transfers angular momentum to the gas via a strong magnetic field in the low plasma- β polar region to force the gas to rotate at

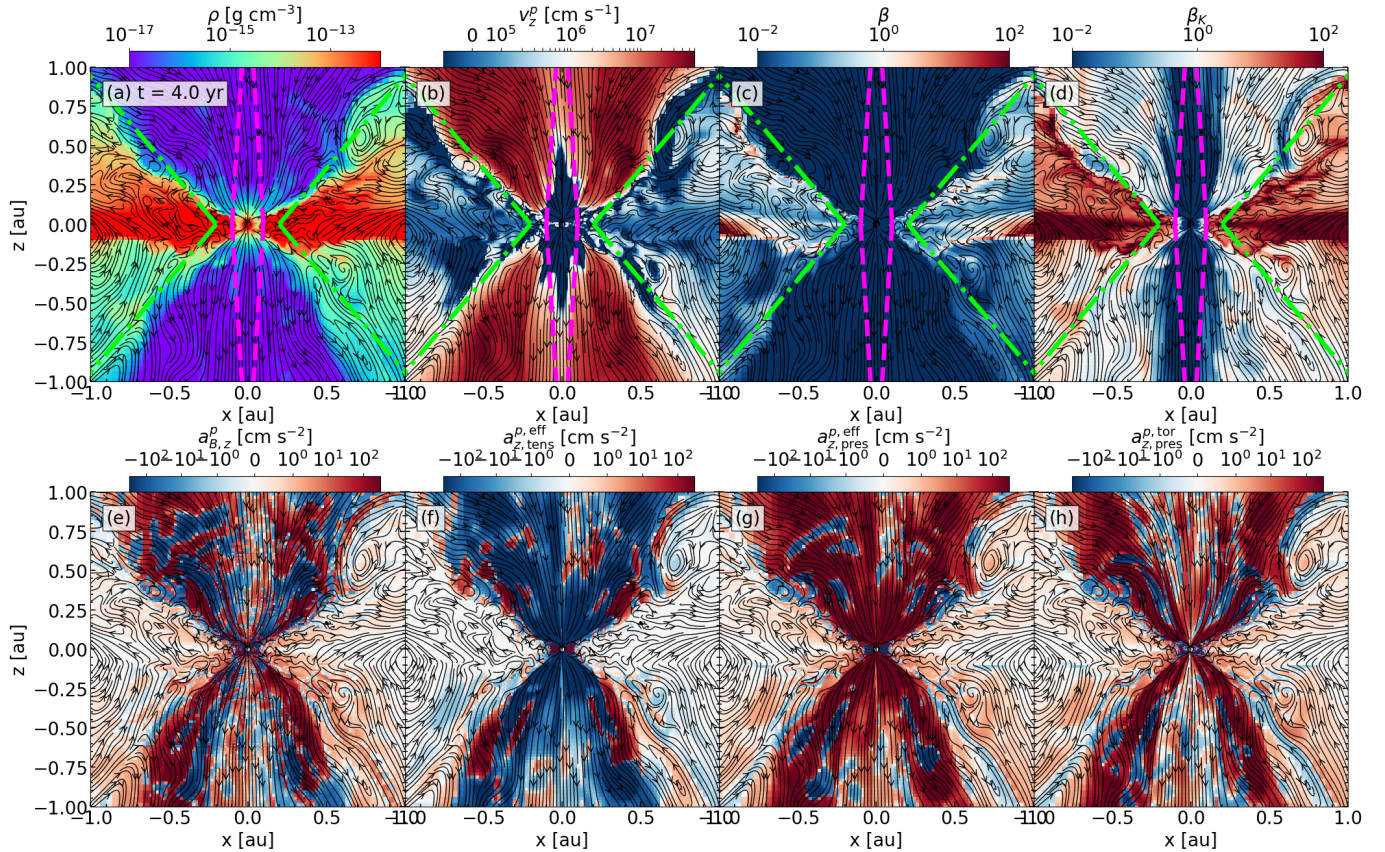


Figure 6. Overview of the jet. Upper panels focus on the magneto-hydrodynamic properties of the jet; lower panels focus on the magnetic forces. **Panels (a) and (b)** show the density and projected \hat{z} -direction (v_z^p , equ. 9) respectively, showing the jet lies in the low-density polar cavity. **Panels (c) and (d)** show the plasma- β (equ. 12) and kinetic- β (equ. 13) respectively, showing the jet is a magnetically-dominated structure. **Panels (e), (f), (g), and (h)** show the total magnetic force, the effective magnetic tension force (equ. 18), the effective magnetic pressure force (equ. 17), and the toroidal magnetic pressure force (equ. 19) respectively.

a super-Keplerian rate. The other end is embedded in the gas-dominated disk, where the gas motion remains nearly Keplerian. The significant differential rotation along this field line, particularly near where the field bends sharply, generates an azimuthal magnetic field, as shown in Figure 7(e).

The differential rotation along this field line generates the azimuthal magnetic field required for jet launching by magnetic pressure, accelerating the gas in the vertical \hat{z} -direction. Consequently, this azimuthal magnetic field is constantly advected away by gas motion. Quantitatively, magnetic field generation and removal in this nearly ideal MHD region (due to ionization by high temperature) are governed by the induction equation (equ. 3). In a cylindrical coordinate, the change in azimuthal magnetic field ($[\frac{\partial B_\phi}{\partial t}]_{\text{tot}}$) can be divided into two processes: generation of B_ϕ from B_z and B_R by differential rotation,

$$\left[\frac{\partial B_\phi}{\partial t}\right]_{\text{gen}} = \frac{\partial(v_\phi B_z)}{\partial z} + \frac{\partial(v_\phi B_R)}{\partial R}, \quad (20)$$

and advection of B_ϕ by gas motion,

$$\left[\frac{\partial B_\phi}{\partial t}\right]_{\text{adv}} = -\frac{\partial(v_z B_\phi)}{\partial z} - \frac{\partial(v_R B_\phi)}{\partial R}. \quad (21)$$

Since the toroidal magnetic field strength (and the magnetic pressure associated with it) is what ultimately powers jet-launching, we focus on the change in toroidal magnetic field strength by defining

$$\frac{\partial|B_\phi|}{\partial t} \equiv \frac{B_\phi}{|B_\phi|} \frac{\partial B_\phi}{\partial t}, \quad (22)$$

where a positive value denotes an increase in the absolute value of the toroidal magnetic field strength and a negative value denotes a decrease. Figure 7(f), (g), and (h) shows $[\frac{\partial|B_\phi|}{\partial t}]_{\text{tot}}$, $[\frac{\partial|B_\phi|}{\partial t}]_{\text{gen}}$, and $[\frac{\partial|B_\phi|}{\partial t}]_{\text{adv}}$ respectively. Although $|B_\phi|$ decreases in magnitude in a large part of the jet-launching region at the time shown, $|B_\phi|$ switches rapidly between net gain and loss of strength over time, resulting in a quasi-steady state. The reader is encouraged to view the animated version of Figure 7 to see this rapid change between gaining and losing $|B_\phi|$.

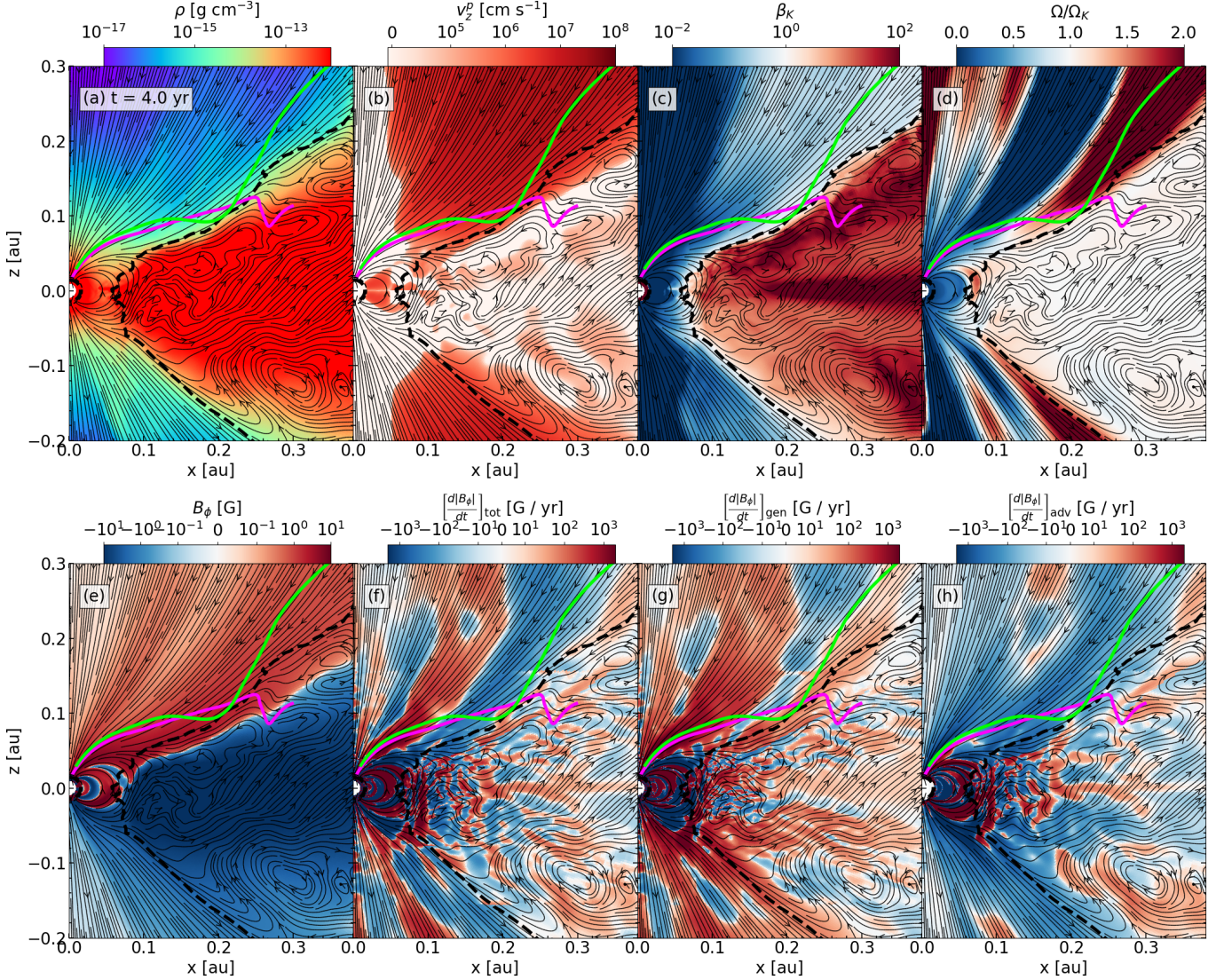


Figure 7. Toroidal magnetic field generation in the jet-launching region. The quantities plotted are azimuthally averaged. **Panel (a) and (b)** show the density and projected \hat{z} -direction velocity (v_z^p , equ. 9) respectively, showing the density structure and the location of the jet. **Panel (c)** shows the kinetic- β (equ. 13), highlighting the transition from the magnetically-dominated polar cavity to the mass-dominated disk. **Panel (d)** shows the angular velocity, normalized by the local Keplerian value. The lower panels show toroidal magnetic field dynamics. **Panel (e)** shows the toroidal magnetic field; **Panels (f), (g), and (h)** show the total change in toroidal field strength (equ. 22), toroidal field generation by differential rotation (equ. 20), and toroidal field advection by flux-freezing (equ. 21) respectively. The black dashed contour highlights the $\beta_K = 1$ surface. The magenta and green field lines are 2D projections of representative 3D field lines shown in Figure 8. An animated version is available at <https://figshare.com/s/e90cdd7f3a49d07ffbc1>. The movie is 25 seconds long, showing the gas properties on the upper panels, and the toroidal field dynamics on the lower panels.

The rapid change in the net change in $\left[\frac{\partial|B_\phi|}{\partial t}\right]_{\text{tot}}$ does not translate to a rapid change in the $\left[\frac{\partial|B_\phi|}{\partial t}\right]_{\text{gen}}$ nor $\left[\frac{\partial|B_\phi|}{\partial t}\right]_{\text{adv}}$. Generation through differential rotation ($\left[\frac{\partial|B_\phi|}{\partial t}\right]_{\text{gen}}$) stays mostly positive on the magnetically dominated side of the $\beta_K = 1$ boundary, and advection through gas motion ($\left[\frac{\partial|B_\phi|}{\partial t}\right]_{\text{adv}}$) stays mostly negative, illustrating the required toroidal magnetic field for jet-

launching is generated in situ by differential rotation along magnetic field lines.

The $\left[\frac{\partial|B_\phi|}{\partial t}\right]_{\text{gen}}$ term being predominantly positive in the jet-launching region indicates that toroidal field generation is not limited to field lines like the magenta field-line highlighted in Figure 7, where one footpoint is anchored in the disk and the other on the star. In fact, any differential rotation between the dense disk gas and the stellar magnetosphere can generate a toroidal mag-

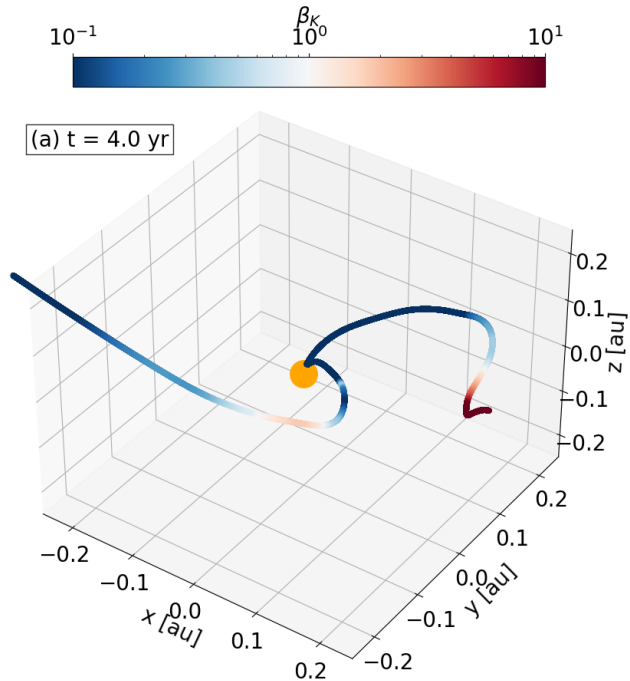


Figure 8. 3D rendition of the two fieldlines highlighted in Figure 7, colored by the local kinetic- β (equ. 13). The yellow sphere at the center represents the star. The magenta fieldline in Figure 7 is located on the right, with one low kinetic- β end on the star and one high kinetic- β end in the disk. The green field line from Figure 7 is shown on the left: most of this field line resides in regions where $\beta_K < 1$, indicating magnetic dominance, except for a localized segment with $\beta_K > 1$, where kinetic energy becomes dominant.

netic field capable of launching an outflow, even if the field line is not fully embedded in the disk. An example of this is shown in Figure 8, where a segment along an otherwise open field line becomes kinetically dominated ($\beta_K > 1$) as it approaches the disk. This local interaction between the disk and the stellar field generates differential rotation, which in turn produces the toroidal field responsible for jet launching.

Similar field lines threading both the disk and the star to the one highlighted in Figure 7(d) can be found in the 3D plot (and the associated animation) of the field lines in the magnetosphere and surrounding regions (see Figure 10 below) along many azimuthal directions, allowing the jet to be driven continuously in the simulation.

Before discussing the release of toroidal magnetic energy during the “fire” phase, we first highlight that the most rapid generation of toroidal field occurs in the polar region near the star. Although this may seem counter-intuitive, since field lines in the magnetically dominated polar region are typically expected to remain relatively straight, this rapid winding arises because the star rotates faster along these field lines than the disk does.

Specifically, for the “two-legged” field lines illustrated in Figures 7 and 8, the footpoint on the disk lies beyond the corotation radius of the star (approximately 0.1 au). As a result, the disk end of the field line rotates more slowly than the stellar end, causing the star to drag the field line forward. This differential rotation leads to significant field twisting near the stellar surface. Although the magnetic deformation is quickly removed by outgoing Alfvén waves (and their associated Poynting flux; see Figure 9 [e, f]) and does not remain near the star, it contributes to the magnetic energy buildup that eventually drives the jet, as we describe in the next subsection.

4.2. Fire: releasing magnetic energy by global field geometry

Another critical consequence of star-disk differential rotation is the emergence of strong current sheets, particularly in the cylindrical \hat{R} direction, which are essential for converting magnetic energy stored in the toroidal field into jet-driving forces. Specifically, the abrupt change in magnetic field geometry by the differential rotation between the star and the disk leads to the generation of a significant radial current density, J_R , expressed as:

$$J_R = \frac{c}{4\pi} \left(\frac{\partial B_z}{\partial \phi} - \frac{\partial B_\phi}{\partial z} \right). \quad (23)$$

This current has two physically distinct contributions:

$$J_{R,1} = \frac{c}{4\pi} \frac{\partial B_z}{\partial \phi}, \quad (24)$$

arises from azimuthal asymmetries in B_z , while the second term,

$$J_{R,2} = -\frac{c}{4\pi} \frac{\partial B_\phi}{\partial z}, \quad (25)$$

stems from vertical gradients in the toroidal magnetic field. Since azimuthal averaging eliminates $J_{R,1}$ by construction, we examine both terms in meridional slices (see Figure 9[a,b]) to evaluate their roles in driving outflows.

For a magnetic force to support jet launching in both hemispheres, the condition $\frac{z}{|z|} J_R B_\phi > 0$ must be satisfied, such that the Lorentz force points away from the midplane. This is generally satisfied when $J_R > 0$, given the sign of B_ϕ in Figure 7[e], which is positive in the polar cavity of the upper hemisphere and negative in that of the lower hemisphere. While $J_{R,2}$ contributes positively to J_R and aligns with the outflow direction, $J_{R,1}$ tends to oppose the jet by introducing a restoring force toward the midplane. Moreover, $|J_{R,1}|$ is typically smaller than $|J_{R,2}|$, so the net current remains positive in the jet-launching region, as shown by the azimuthally-averaged J_R in Figure 9(c).

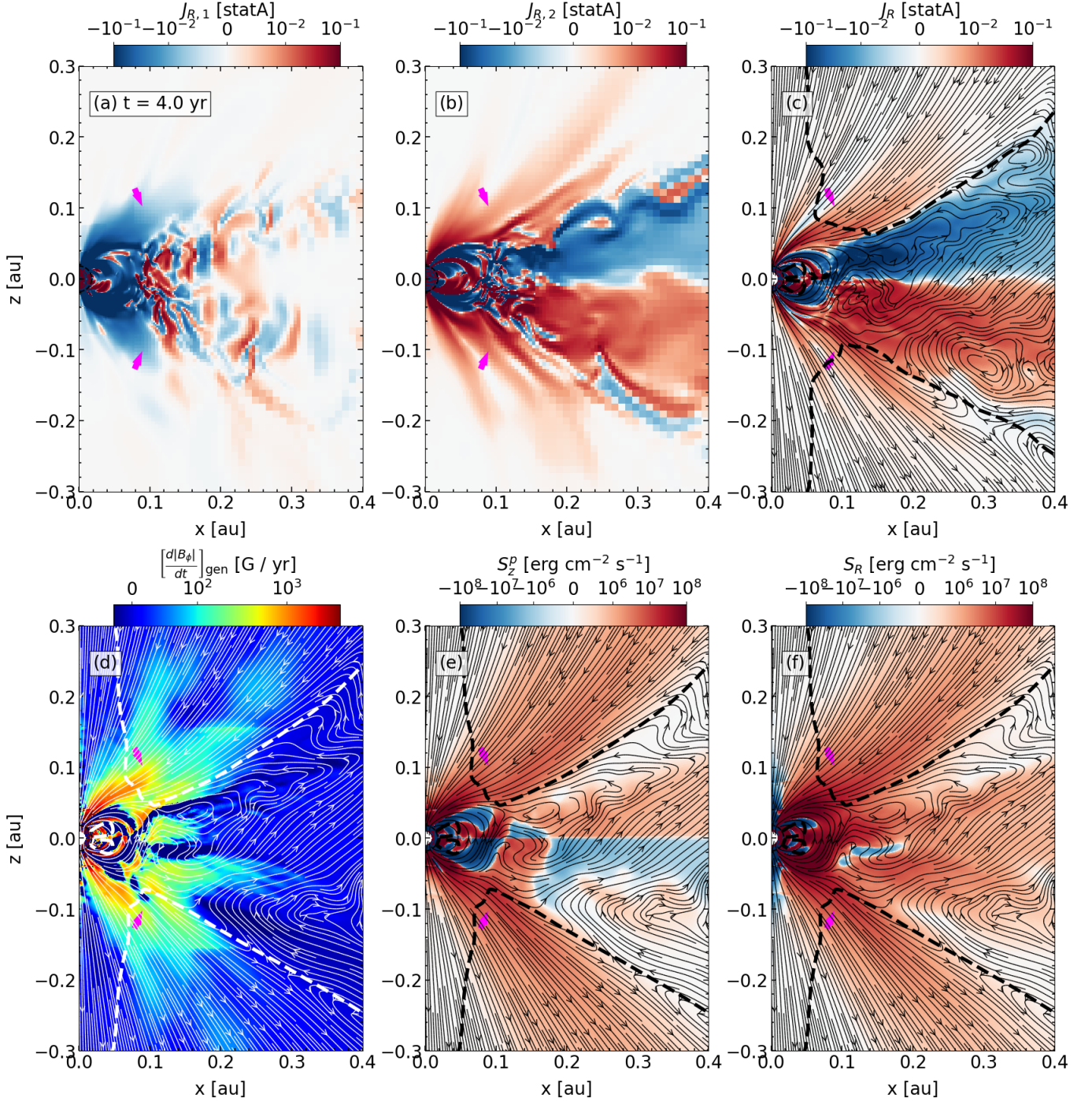


Figure 9. Magnetic energy evolution in the jet-launching region. The top panels illustrate the cylindrical \hat{R} -direction current and its components. Given the toroidal magnetic field structure (Figure 7[e]), a positive current is required to exert a force directly away from the disk. **Panels (a) and (b)** show meridional slices of the two components of the \hat{R} -directed current (equ. 24 and 25), respectively. The component due to azimuthal asymmetry (equ. 24) points toward the midplane, while the component arising from global field geometry (equ. 25) points away from the disk. **Panel (c)** shows the azimuthally averaged current at a representative time, revealing a positive current along the surfaces of both the magnetosphere and disk—sufficient to drive outflows. To reduce transient effects and emphasize large-scale features, panels (d), (e), and (f) present time-averaged (over ± 0.1 yr centered on 4.0 yr) and azimuthally averaged quantities. **Panel (d)** shows toroidal field generation concentrated along narrow streams at the magnetosphere and disk surfaces, highlighting the origin of the current. **Panels (e) and (f)** display the projected Poynting flux in the \hat{z} - and \hat{R} -directions, respectively, demonstrating how magnetic energy generated near the star is transported outward to power the jet. The dashed contours in panels (c)–(f) outline the approximate extent of the jet.

This jet-driving current is generated locally along the surface of the closed magnetosphere and the disk as a consequence of the rapid changes in the toroidal magnetic field geometry in the vertical direction. As discussed in Sec. 4.1, differential rotation between the star and the disk twists magnetic field lines most effectively when the field line has one end rooted in the star and the other embedded in the disk. A comparatively strong toroidal field is produced in this narrow layer where such “two-legged” field lines reside. Above this region, in the low-density polar cavity, the strong magnetic field keeps the fieldlines roughly poloidal, and the toroidal component remains weak. Below this region is the mass-dominated disk, where the magnetic effect is more diminished, providing a solid foundation for the outflow.

As a result, the field lines within this intermediate layer, subject to significant differential rotation, are continually over-twisted relative to those above and below. This localized over-twisting establishes steep vertical gradients in the toroidal magnetic field, giving rise to a strong radial current sheet (J_R) essential for jet launching. Because this differential twisting is inherently highly variable in space and time, we illustrate it in Figure 9(d) using the azimuthally and temporally averaged quantity $\left[\frac{\partial B_\phi}{\partial t}\right]_{\text{gen}}$. The colormap highlights the toroidal magnetic field’s generation rate in the layer above the closed magnetosphere and disk atmosphere, with more positive values indicating faster local toroidal field generation. The peaks in the toroidal field generation rate, pointed by arrows in Figure 9(d), align with the location of the J_R current sheet at the disk surface. However, as shown in Figure 9(d), the gas in the most rapid toroidal field generating region near the star is infalling, rather than outflowing (the outflow region is outlined in white in Figure 9[d]). This raises a natural question: how does the energy generated in this inner region reach the outflow zone to drive the jet?

The answer lies in the Poynting flux, defined as

$$\mathbf{S} = -\frac{1}{4\pi}(\mathbf{v} \times \mathbf{B}) \times \mathbf{B}, \quad (26)$$

where \mathbf{v} and \mathbf{B} are the gas velocity and magnetic field respectively. The Poynting flux enables magnetic energy to travel faster than the gas itself. Even in regions of infall, magnetic fields can transport energy outward, effectively “advecting” it upstream into the jet-launching region. To illustrate this process, we show in Figure 9(d, e) the Poynting flux in \hat{z} direction ($S_z^p = z/|z| \mathbf{S} \hat{z}$, projected in the same way as the \hat{z} direction velocity v_z^p , equ. 9) and cylindrical- \hat{R} directions ($S_R = \mathbf{S} \hat{R}$), respectively. Even in the infall region around the polar axis,

magnetic energy can be transported away from the star’s vicinity to the outflow region.

In summary, the combined effect of the J_R current sheet (Figure 9[c]) and the amplified toroidal field (Figure 7[e]) generates a vertical (\hat{z} -direction) magnetic force, accelerating gas to high poloidal velocities.

4.3. Reload: replenishing jet gas by magnetic reconnection

The “two-legged” magnetic field lines, such as those shown in Figure 7(e), stretch and may open during outflow launching. To sustain a continuous jet (Figure 1), these field lines must reconnect and revert to a “two-legged” configuration, “reloading” with mass by magnetic reconnection between oppositely directed field lines. As discussed in Sections 3.1 and 3.3, the global magnetic topology at late times when a persistent outflow is launched consists of downward-pointing original magnetospheric field lines that are opened but remain connected to the star (referred to as “the opened stellar field lines” for short) and upward-pointing original magnetospheric field lines that are opened but thread through the (inner) disk (but not the star). These oppositely directed open field lines are expected to preferentially reconnect at their interface. Although individual reconnection events are difficult to isolate in a highly variable 3D system, we present qualitative evidence below to confirm reconnection along this boundary.

Figure 11(a)-(d) presents the time evolution of the azimuthally averaged radial velocity v_r at $t = 3.7, 3.8, 3.9,$ and 4.0 yr. To track the evolution of the magnetic field, we trace field lines using contours of the radial magnetic flux:

$$\Phi_{B,r}(r, \theta) = \int_0^\theta \int_0^{2\pi} B_r r^2 \sin \theta' d\phi d\theta', \quad (27)$$

where constant $\Phi_{B,r}$ contours approximate field line locations, as indicated by the black dashed curves in Figure 11. These contours represent azimuthally averaged field configurations, capturing only the global magnetic evolution. In reality, three-dimensional reconnection events occur on much shorter timescales. Between $t = 3.7$ yr (panel [a]) and $t = 4.0$ yr (panel [d]), the same averaged field line transitions from an extended state to a more compact (lower altitude) configuration. Given the continuous outflow during this interval, the contraction of the averaged field line suggests magnetic reconnection.

Reconnection primarily occurs along the $B_r = 0$ boundary (highlighted by the magenta contour in Figure 11) where the open field lines threading the star and disk meet. This process regulates the magnetic configuration at high altitudes, maintaining a quasi-steady

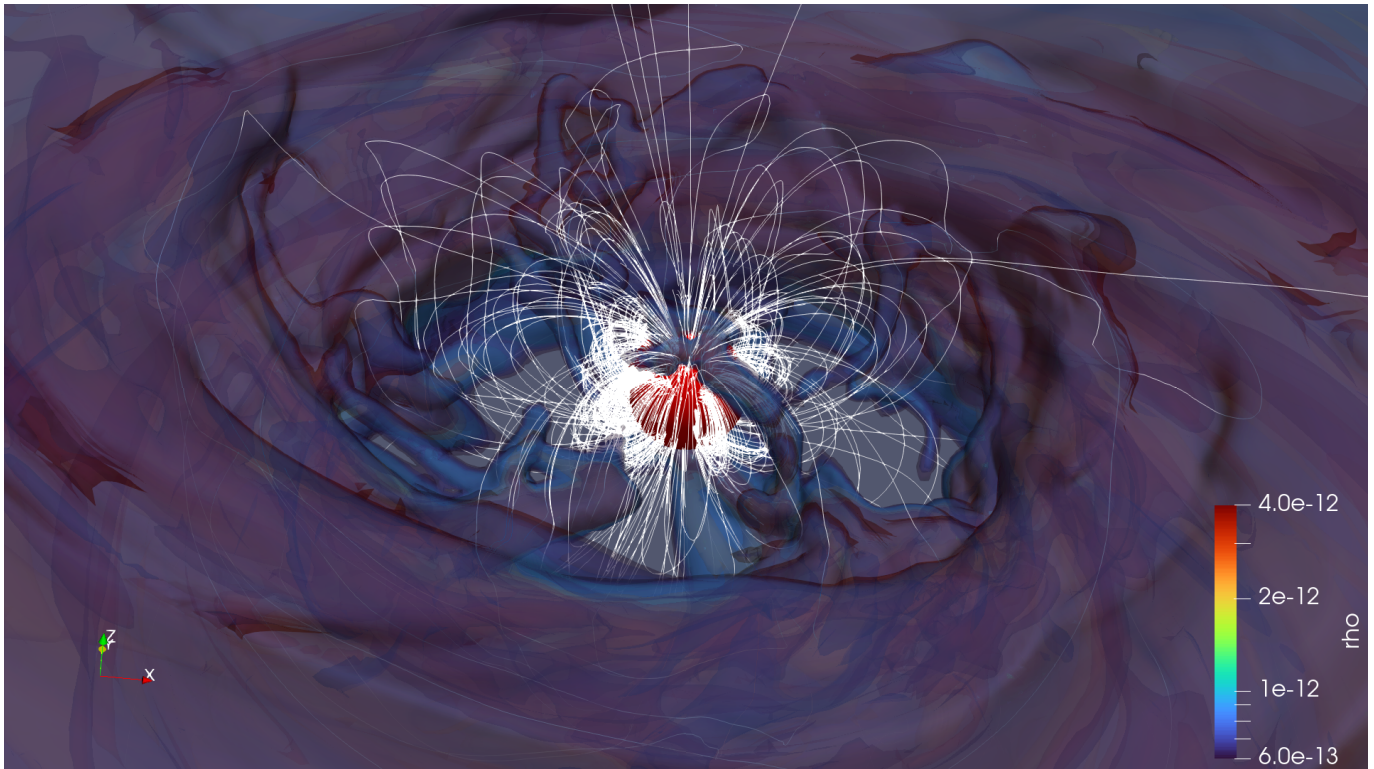


Figure 10. 3D rendition of the protostar, accreting magnetosphere, and magnetic field lines. The disk is shown as semi-transparent density isosurfaces at around 10^{-12} g cm^{-3} . The protostar is represented by the central red solid sphere. White lines depict magnetic field lines, including permanently closed magnetospheric loops and twisted field lines resulting from magnetosphere–disk interactions (e.g., the prominent twisted fieldline near the top-center of the image). An animated version of this figure is available at: <https://figshare.com/s/413012328cf225f86a67>. The movie is 27 seconds long, showing the magnetic field lines near the magnetosphere.

state in the opened stellar magnetic flux (Figure 3[a]). In three dimensions, magnetic field stretching and localized reconnection events occur simultaneously at different heights and across multiple azimuthal sectors, ensuring quasi-continuous jet ejection.

To summarize, jet launching operates through a “load-fire-reload” cycle driven by differential rotation between the star and disk. The twisting of magnetospheric field lines amplifies the toroidal magnetic field, generating a strong current sheet that accelerates the jet via the magnetic pressure force. Reconnection near the field reversal interface then resets the system, reforming field lines connecting the star and disk and reloading them with disk material for the next cycle. This process sustains a continuous outflow.

5. DISCUSSION

5.1. Magnetospheric accretion and outflow

Although magnetospheric accretion is not the focus of this paper, we describe its general properties to set the stage for comparison with other jet-launching mechanisms.

Figure 12(a) shows a 3D rendering of the accretion streams onto the star (the red sphere at the center). The accretion streams are filamentary and follow the magnetospheric field lines. These “finger-like” accretion patterns result from the “interchange instability,” a form of Rayleigh-Taylor instability in a magnetically dominated environment. Gas from the mass-dominated disk is loaded onto the strong magnetic field and subsequently accreted onto the star following the stellar magnetic field lines. This mechanism is established by theory (J. Arons & S. M. Lea 1976; H. C. Spruit et al. 1995) and simulations (M. M. Romanova et al. 2008; A. A. Blinova et al. 2016; S. Takasao et al. 2022; Z. Zhu et al. 2024).

These accretion streams originate from a mass-dominated disk whose boundary with the magnetically dominated magnetosphere marks the magnetospheric truncation radius R_T . We estimate the location of R_T in two ways.

First, we follow Z. Zhu (2025) and define the corotation radius analytically using the stellar parameters.

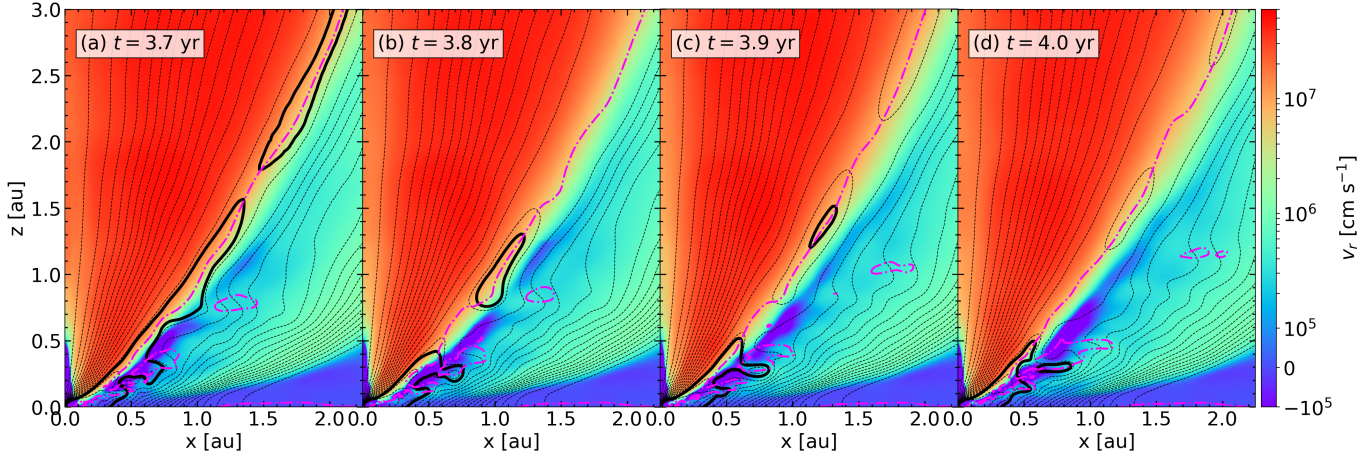


Figure 11. Illustration of the “reload” stage where magnetic reconnection resets the field geometry. While individual reconnection event occurs rapidly and is unrealistic to show explicitly in 3D simulations, we illustrate the cumulative effect using azimuthally integrated magnetic flux surfaces. The panels present a time sequence of the flux surface evolution. The background color shows the radial velocity in spherical coordinates (v_r), highlighting the jet’s location. Black lines represent azimuthally averaged magnetic flux surfaces, which can also be interpreted as approximate magnetic field line locations. The thick black line shows magnetic reconnection by tracing a representative field line along the $B_r = 0$ surface, which is marked by the magenta dash-dot line.

The corotation radius is given by

$$R_{T,\text{ana}} = R_* \left(\frac{B_*^4 R_*^5}{2GM_* \dot{M}} \right)^{1/7} = \left(\frac{\bar{m}^4}{2GM_* \dot{M}} \right)^{1/7}, \quad (28)$$

where B_* and R_* are the magnetic field strength on the stellar surface and radius of the star, respectively, M_* , \dot{M} are the stellar mass and mass accretion rate, respectively. \bar{m} is the coefficient used in setting the strength of the stellar magnetosphere (equ. 8). Note that our expression is slightly different from the one in Z. Zhu (2025) because of the difference in the unit system. Using our simulation parameters and $\dot{M} = 10^{-7} M_\odot \text{ yr}^{-1}$ for the accretion rate at late times ($t \gtrsim 3$ yr) when the system settles to a quasi-steady state (see below, and Figure 12), the truncation radius $R_{T,\text{ana}} \approx 0.088$ au.

Second, we follow S. Takasao et al. (2022) and define R_T as the smallest radius where $\beta_K = 1$. In our model, R_{T, β_K} settles to a value ≈ 0.082 au ($\approx 5R_*$) at late times, slightly lower than the analytic estimate. Since the accretion stream is filamentary (Figure 12[a]), it is not surprising that the material with $\beta_K = 1$ can penetrate slightly into the magnetosphere. The truncation radius is comparable to the corotation radius ≈ 0.1 au. Our R_T is larger than S. Takasao et al. (2022) compared to the stellar radius, since our stellar magnetic field is stronger than theirs.

Most of the mass is accreted along magnetic field lines onto the star away from the midplane. To illustrate the landing locations of the gas on the star, we show in Figure 12(b) the averaged mass accretion rate per unit area at different polar angles $\frac{\partial \dot{M}}{\partial A}(\theta)$ between 3.0 yr and

5.5 yr in our model measured right outside r_{fix} (sec. 2) at 0.02 au. Most accretion occurs around $\sim 20^\circ$ – 40° from the polar axis, while the accretion around the midplane ($\theta = 90^\circ$) is negligible.

The highly filamentary high-altitude accretion does not imply a strong variation in the accretion rate. Figure 12(c) shows that throughout the later stage of the simulation between 3.0 yr and 5.5 yr, the total mass accretion rate remains around $1 \times 10^{-7} M_\odot \text{ yr}^{-1}$. In comparison, the jet outflow rate, defined as the total mass flux at ± 5 au with $v_z^p > 10^7 \text{ cm s}^{-1}$, is about $2 \times 10^{-9} M_\odot \text{ yr}^{-1}$, around 2% \sim 5% of the gas accretion rate. The total mass outflow rate, measured at ± 5 au with gas velocity $> 10^6 \text{ cm s}^{-1}$, is around $4 \times 10^{-8} M_\odot \text{ yr}^{-1}$. The total outflow rate is about 40% of the total accretion rate, similar to the ratio in S. Takasao et al. (2022) and Z. Zhu et al. (2024), although the exact values differ mainly due to the difference in the chosen stellar magnetosphere magnetic field strength.

The outflow carries angular momentum. To connect the angular momentum transported with the disk Keplerian angular momentum, we define the “Keplerian angular momentum radius” following Y. Tu et al. (2025a)

$$R_a = \frac{1}{GM} \left(\frac{\Phi_l}{\Phi_m} \right)^2, \quad (29)$$

where Φ_l and Φ_m are the angular momentum flux and mass flux in the outflow, respectively. Figure 12(d) shows R_a for the jet and the disk wind, respectively, measured at $z = 5$ au. The jet $R_a \approx 0.6$ au, much larger than its launch radius $\lesssim 0.2$ au. This shows an abundance of angular momentum carried by the jet, initially

stored in the electromagnetic form associated with the twisting of the field lines. The disk wind $R_a \approx 1.3$ au, slightly larger than its launching radius $\lesssim 1$ au.

Both the jet and the disk wind carry significant angular momentum. In the following section (sec. 5.2), we will compare the accretion and outflow properties with those driven by the disk through the avalanche-accretion stream. Since the key distinction between the disk-driven outflow and our model is the presence of a stellar magnetosphere, we will discuss its impact on the overall dynamics of the system.

5.2. Comparing to the disk-field-only jet model

An alternative jet-launching mechanism involves jets driven solely by the disk magnetic field. Y. Tu et al. (2025b) and Y. Tu et al. (2025a) model outflows in the absence of a stellar magnetosphere and identify a mechanism in which jets are powered by the so-called “avalanche-accretion stream” in the magnetically elevated atmosphere of the disk. In this section, we compare the outflows driven by stellar magnetosphere-disk interactions with those produced by the disk magnetic field alone.

To set the stage for this comparison, we first summarize the disk-field-only jet-launching mechanism described in Y. Tu et al. (2025b) and Y. Tu et al. (2025a). In this scenario, the disk is threaded by a large-scale, open vertical magnetic field. Due to differential rotation and magnetic field geometry, the azimuthal magnetic field B_ϕ must switch sign somewhere between the upper and lower hemispheres, typically along the disk surface on one side. This sign reversal leads to strong azimuthal magnetic braking, which removes angular momentum and drives an avalanche-accretion stream along the disk surface. The differential rotation between this stream and the open field lines rapidly amplifies the toroidal magnetic field, generating strong toroidal magnetic pressure that lifts a portion of the accretion stream vertically, launching a jet. A similar process drives a slower, more mass-loaded disk wind at larger cylindrical radii, though this does not require the formation of an avalanche-accretion stream. Some regions of the inner disk wind can be magnetorotational instability (MRI)-active, where turbulent gas is lifted to high altitudes before merging with the disk wind.

On the side of the disk without the azimuthal field sign change, the avalanche-accretion stream does not form, but jets can still emerge if the polar region remains relatively mass-free. However, MRI-active turbulent disk winds can fill the polar region with turbulent gas in many cases, overloading the outflow and effectively choking the jet. As a result, disk-field-only mod-

els frequently produce one-sided jets (see also, e.g., W. Béthune et al. 2017; D. Takaishi et al. 2024).

A key distinction between the disk-only model and our magnetosphere-disk model is the persistence of a bipolar jet in our simulations (see Figure 1). This difference arises from the global magnetic field geometry. In the presence of a stellar magnetosphere, the opening of the outer magnetosphere establishes a poloidal magnetic field structure with opposite directions between the polar region and its immediate surroundings. With differential rotation between gas at different altitudes, this configuration produces a quadripartite global toroidal magnetic field topology, with bipartite in each hemisphere in the case of a rapidly spinning stellar magnetosphere (as shown in Figure 13). Magnetic reconnection occurs along the boundary between the two magnetic partitions in each hemisphere, naturally limiting the disk’s vertical expansion. This effect is analogous to the role of avalanche accretion streams in the disk-only models. As a result, the magnetic configuration inherently supports the formation of a bipolar jet. In contrast, the disk-field-only model maintains a bipartite global toroidal field geometry (see, e.g., Figure 9 in Y. Tu et al. 2025a), meaning that the toroidal field remains unipartite in each hemisphere. As a result, the avalanche accretion stream can develop only in the hemisphere where the toroidal field reverses direction. This asymmetry leads disk-field-only models to preferentially launch unipolar jets.

Another key distinction lies in how the toroidal magnetic field is generated. While both models rely on toroidal magnetic pressure to power the jet, the underlying mechanism for twisting the field differs significantly. In the disk field only model, the toroidal field is amplified by the differential rotation between the avalanche accretion stream of the disk surface and the slower-rotating gas above (and below) it. This configuration results in a toroidal twisting of the field where a faster-rotating layer below winds up a slower-rotating layer above.

In contrast, the disk-magnetosphere model produces the toroidal field in an opposite manner. Here, strong magnetic field lines anchored to the rotating star transfer angular momentum to the disk surface, spinning up the upper layers of the disk relative to the denser regions below. As a result, a toroidal field is generated by the differential rotation between the faster-rotating upper layers and slower-rotating lower layers of the disk.

There are several important consequences of these differences in the generation of toroidal magnetic fields. One immediate effect is on the geometry of the poloidal magnetic field that channels the jet. In the disk-field-only model, the avalanche-accretion stream drags mag-

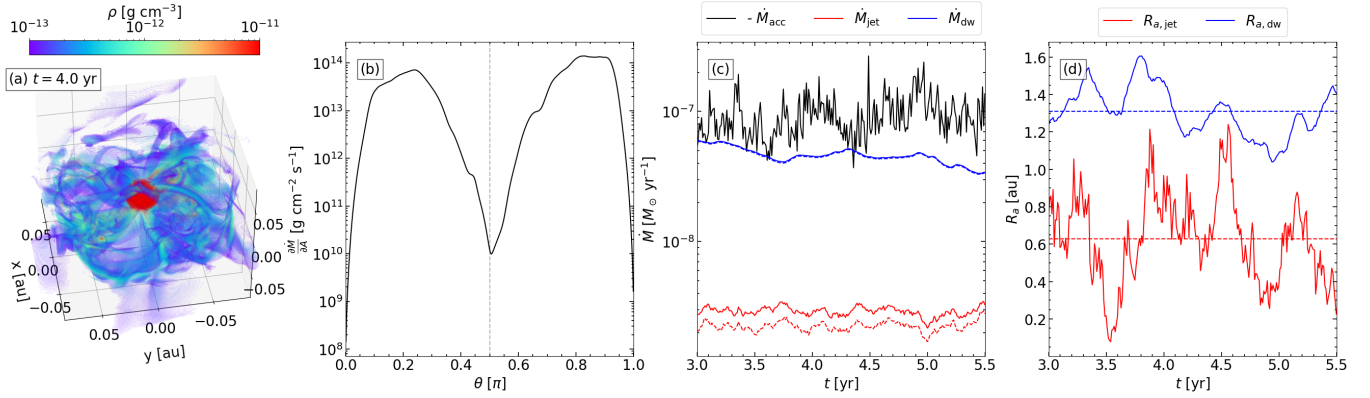


Figure 12. Accretion and outflow properties. **Panel (a)** shows a 3D rendition of the accretion streams by only choosing cells with real $\rho > 10^{-13}$ g cm $^{-3}$ and kinetic- $\beta < 1$. **Panel (b)** quantifies the landing locations of the mass accretion rate streams on the star at each polar angle, showing off-midplane accretion along magnetosphere fieldlines. **Panel (c)** shows the total mass accretion rate (black line on top), jet outflow rate (red line at the bottom), and the disk wind outflow rate (blue line in the middle). The red dashed line is the jet outflow rate using the real gas only, showing the density floor’s minimal effect on the outflow. **Panel (d)** shows the “Keplerian angular momentum radius” (R_a , equ. 29) of the jet (lower red line) and the disk wind (upper blue line). The horizontal dashed lines mark the averaged R_a over the time shown.

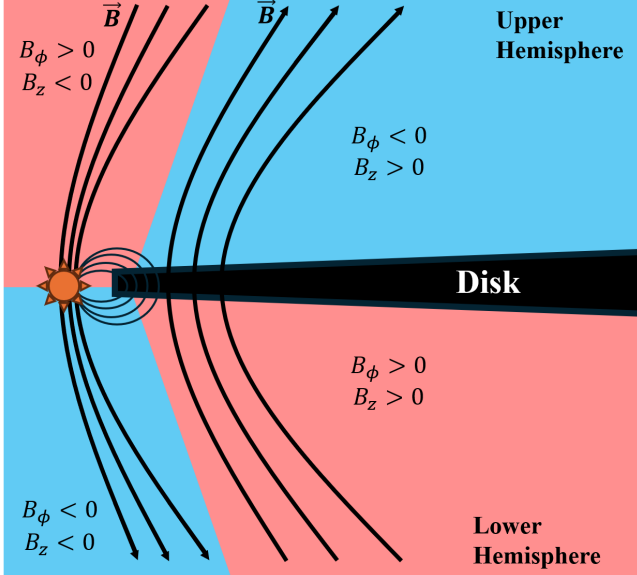


Figure 13. Illustration of the resulting large-scale toroidal magnetic field configuration, shaped by the poloidal field geometry established through the presence and partial opening of the rotating stellar magnetosphere. In contrast to the disk-only case (Y. Tu et al. 2025a), where the magnetic field direction reverses in only one hemisphere, both the poloidal and toroidal components exhibit reversal in both the upper and lower hemispheres in the case with a stellar magnetosphere.

netic field lines inward, resulting in an inward-pinned poloidal field configuration (see Figure 5 in Y. Tu et al. 2025b). In contrast, in the magnetosphere-disk model, the pinching point of the field moves outward, leading to an outward-pinned poloidal magnetic field structure (Figure 7).

The difference in magnetic field geometry stems from differences in the power source of the jet. In the disk-field-only model, the disk itself provides all the energy and angular momentum for the outflow. In contrast, in the magnetosphere-disk model, the field lines anchored on the rotating star provide an additional source of energy and angular momentum to power the jet. In addition, once opened, the magnetosphere supplies the inner disk with a much stronger open poloidal field than in the disk-field-only case, and provides a global field configuration with oppositely directed open poloidal fields near the (elevated) disk surface that is conducive to magnetic reconnection and jet mass loading. As a result, jets in the magnetosphere-disk model are both more energetic and more massive than those in the disk-field-only model from Y. Tu et al. (2025a). Specifically, the jet in our simulations reaches velocities of several hundred km s $^{-1}$, compared to ≈ 100 km s $^{-1}$ in the disk-field only case. The mass outflow rate is also higher, with $\dot{M}_{\text{jet}} \approx 2 \times 10^{-9} M_{\odot} \text{ yr}^{-1}$ compared to $\approx 2 \times 10^{-11} M_{\odot} \text{ yr}^{-1}$. Additionally, the jet carries more angular momentum, with the Keplerian angular momentum radius (equ. 29) of $R_a \approx 0.6$ au, compared to 0.3 au in the disk-field-only model.

Similarly, the disk wind in the magnetosphere-disk model is stronger than in the disk-field-only model. This enhancement arises partly from the additional magnetic field strength in the disk due to the opening of the stellar magnetosphere. Moreover, some angular momentum in the disk wind originates from the star itself. When the magnetic field transfers energy and angular momentum to the jet, a portion of that angular momentum is fed into the disk. Although this effect is relatively mi-

nor in terms of driving outflows (since the disk remains gas-dominated), it contributes to the overall angular momentum budget of the disk wind.

In summary, the stellar magnetosphere plays two critical roles in shaping the outflow. First, the opening of the magnetosphere increases the field strength in the jet-launching inner disk region and imposes a global field geometry that is conducive to jet mass loading through reconnection and resistant to the choking of the jet by the disk wind. Second, by transferring energy and angular momentum from the rotating star to the outflow, the magnetosphere strengthens both the jet and the disk wind, making them more energetic and angular-momentum rich than in the disk-field-only scenario.

5.3. Comparison with previous 2D models

The “load-fire-reload” jet-launching mechanism in our model shares many similarities with previous 2D models. Studies such as A. P. Goodson & R. M. Winglee (1999); T. Kuwabara et al. (2000); C. Fendt & D. Elstner (2000); S. Matt et al. (2002); M. M. Romanova et al. (2005); C. Fendt et al. (2011); M. Čemeljić et al. (2013); C. Zanni & J. Ferreira (2013) also observed the cyclic behavior of magnetic field lines, where outflows are launched before the field resets to its initial configuration for the next cycle. The formation of a current sheet due to differential rotation, as described in Sec. 4.2, is conceptually similar to the current sheet discussed in D. A. Uzdensky (2002).

However, our model differs from these 2D studies in two key ways: (1) the inclusion of the azimuthal dimension, and (2) the longer simulation runtime, allowing the system to reach a quasi-steady state. The additional dimension enables axisymmetric processes to break down, while the extended simulation duration ensures that transient effects from the initial conditions dissipate. These differences lead to three main consequences.

First, the jet can be launched continuously (see Figure 1) because magnetic expansion and reconnection can occur simultaneously at different azimuthal angles. This sustained flaring and reconnection stabilize the system into a quasi-steady state in the late simulation stages. Additionally, mass loading onto the jet-launching field lines becomes more efficient due to reconnection along the disk surface-polar cavity boundary. The frequent localized magnetic reconnection and field expansion events alleviate the need for the global large-scale episodic outbursts often seen in 2D simulations.

Second, the magnetic field geometry associated with jet launching differs from 2D models. In our simulation, the field does not need to fully reconnect into

closed loops across the disk midplane before another jet-launching event can occur: the only requirement is that the opened magnetosphere field lines threading the star touch and at least shallowly embedded in the disk atmosphere (as exemplified by the green and magenta field lines in Fig. 7); the touch of the disk is facilitated by the elevation of the atmosphere of the disk, driven by the amplification of the toroidal field in the inner ideal MHD part of the disk (J. S. Oishi et al. 2020). As a result, only localized reconnection along the surface of the highly elevated and highly dynamic disk atmosphere is necessary to generate a jet, rather than global reconnection involving a coherent poloidal field threading the disk midplane.

These differences, particularly the suppression of large-scale temporal variations, are consistent with the findings of S. Takasao et al. (2022). While 2D models are valuable for developing first-step theories and characterizing general properties, these differences highlight the crucial role of 3D models in capturing additional key ingredients of the outflow-launching process.

5.4. Connection to the axisymmetric steady-state outflow

Although the outflow launching mechanism in our model is highly variable in space and time, it is still valuable to put our model in the context of the axisymmetric steady-state wind theory.

Four quantities are conserved along a magnetic field line in the axisymmetric steady-state wind model. However, since our jet-launching mechanism (Sec. 4) involves the opening and reconnection of magnetic field lines, this “along a magnetic field line” picture is not strictly applicable. Nevertheless, we can reinterpret these conserved quantities to gain insight into the properties of the outflow.

The first conserved quantity,

$$k = \frac{4\pi\rho v_{\text{pol}}}{B_{\text{pol}}}, \quad (30)$$

characterizes the degree of mass loading of the outflow. Physically, k is the 4π times the ratio between the outflow mass flux $\dot{M}_{\text{out}} = \rho v_{\text{pol}} A$ and the magnetic flux $\Phi_B = B_{\text{pol}} A$, where A is an area element perpendicular to the poloidal field.

The second is the conserved angular velocity:

$$\omega_s = \frac{v_\phi}{R} - \frac{k B_\phi}{4\pi\rho R}, \quad (31)$$

where the first term is the angular velocity of the gas and the second term can be interpreted as the magnetic contribution to the conserved angular velocity.

Similarly, the third quantity is the angular momentum, and the two terms are the angular momenta carried by the gas and magnetic field, respectively:

$$l = Rv_\phi - \frac{RB_\phi}{k}. \quad (32)$$

The last is the energy

$$E = \frac{1}{2}v^2 + \Phi - \frac{\omega_s RB_\phi}{k} + h, \quad (33)$$

which is derived from Bernoulli’s equation. The four terms are energy carried by gas advection, gravity, magnetic field, and gas internal energy, respectively. Since thermal energy is negligible in the outflow (plasma- $\beta \ll 1$, Figure 4), the energy carried by the gas is essentially its kinetic energy.

To connect our model with these quantities, we show in Figure 14 the mass-weighted averaged quantities at every height z in the jet, defined as gas moving at a speed $v_z^p > 10^7$ cm s $^{-1}$. Note that while this analysis does not trace along individual magnetic field lines, the mass-weighted averaged quantities offer insight into the jet properties.

Figure 14(a) shows k , which is roughly constant along the jet. This indicates that the mass loading of the outflow remains approximately the same as the jet propagates outward.

Figure 14(b), (c), and (d) show ω_s , l , and E , and their gas and magnetic component, respectively. While the magnetic field dominates ω_s (the magnetic field is mostly toroidal) at large distances, gas dominates both angular momentum l and energy E . Only around the base of the jet $\lesssim 2$ au does the magnetic field dominate in angular momentum and energy, suggesting that energy and angular momentum are transferred from the magnetic field to the gas as the outflow propagates outward, and the outflow on the large scale is gas-dominated. These findings are consistent with, and similar to, the analysis along the field line in Y. Tu et al. (2025b,a); J. Jacquemin-Ide et al. (2021).

To further quantify the outflow properties, we show in Figure 14(e) the plasma- β , kinetic- β (β_K), and the poloidal kinetic- β , defined as

$$\beta_{K,\text{pol}} = \frac{\rho v_{\text{pol}}^2}{B_{\text{pol}}^2/4\pi}. \quad (34)$$

While plasma- β is confirmed to be much less than order unity, kinetic- β stays above 1 beyond the launching zone, emphasizing the gas dominance at large heights. The $\beta_{K,\text{pol}}$ is larger than β_K , highlighting the dominance of the poloidal gas motion over the poloidal magnetic field. Figure 14(f) further quantifies the velocity and

magnetic field geometry, showing the ratio between the toroidal and the poloidal velocity or magnetic field. At a large height, the poloidal velocity dominates the toroidal velocity, but the magnetic field is mostly toroidal. This is consistent with the observation in Figure 1(3D figure), where the streamlines (black lines) are mainly poloidal, while the magnetic fields (white) are mainly toroidal on the plotted scales.

6. CONCLUSIONS

We performed a 3D non-ideal MHD simulation of outflow-launching involving a rotating protostar, the stellar magnetosphere, the circumstellar disk, and open magnetic field lines threading the disk. In our model, a fast, collimated bipolar jet is launched, surrounded by a slower, wider, but more mass-loaded disk wind. Our main conclusions are as follows.

1. During the early stages of the simulation, the stellar magnetosphere opens up, forming three distinct magnetic regions: (1) a polar region of open stellar field lines extending outward from the star; (2) a lower-latitude region of open stellar field lines threading into the disk, with field directions opposite to those in the polar region; and (3) an intermediate zone between the two, where oppositely directed poloidal magnetic fields coexist, a crucial region in the jet-launching process. In the inner disk, the open stellar field overwhelms the native disk field, facilitating the launch of a magnetically driven disk wind.
2. The jet is driven by toroidal magnetic pressure through a “load–fire–reload” cyclic process primarily involving magnetic field lines that connect the star and the vertically elevated disk surface. In the “load” stage, differential rotation along a magnetic field line between the star and the disk transfers rotational energy into the magnetic field, amplifying the toroidal component along field lines. This twisting is especially pronounced in a layer along the surfaces of the stellar magnetosphere and the disk, where it builds up a strong toroidal field. As the toroidal field strengthens in that layer, it generates a current in the cylindrical- \hat{R} direction. This current, in turn, produces a vertical Lorentz force that propels the gas upward: the “firing stage” of the cycle. The release of toroidal magnetic energy drives the gas to expand in the \hat{z} direction, launching the jet. Eventually, magnetic reconnection along the jet-launching field lines resets the field configuration, returning the magnetic field lines to the “two-legged” configuration, anchored at both the star and disk, ensuring that the

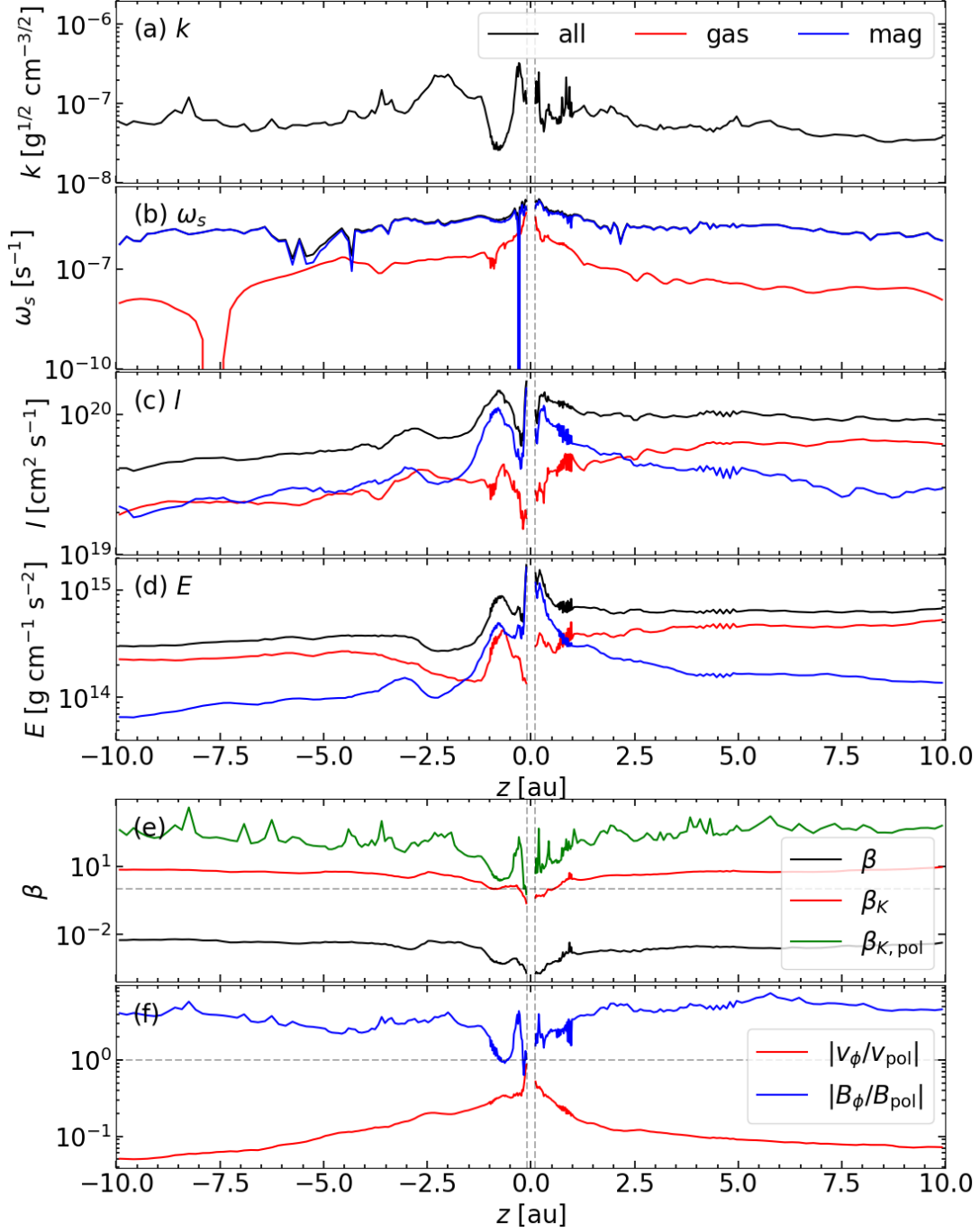


Figure 14. Mass-weighted average conserved quantities (upper four panels) and outflow properties (lower two panels) at different heights. **Panels (a), (b), (c), and (d)** show the mass loading parameter (equ. 30), angular velocity (equ. 31), angular momentum (equ. 32), and energy (equ. 33) respectively. **Panel (e)** shows the plasma- β (equ. 12), kinetic- β (equ. 13), and the poloidal kinetic- β (equ. 34). **Panel (f)** shows the ratios of toroidal to poloidal components for both velocity and magnetic field, illustrating the changing dominance of flow and field geometry with height.

system is continually “reloaded” for subsequent episodes of jet-launching.

3. Compared to the disk-only model presented in Y. Tu et al. (2025a), both the jet and disk wind are stronger in the stellar magnetosphere model, exhibiting higher velocities and greater mass fluxes. The disk wind is stronger because the partially opened stellar magnetosphere provides additional open magnetic flux to the disk, which increases the field strength in the inner disk and facilitates a stronger disk wind. The rotating star provides an additional power source to power the jet, which, together with the stronger open magnetic field in the polar cavity, helps drive a stronger jet in the magnetosphere model.
4. The jet tends to be bipolar in the magnetosphere model, in contrast to the disk-only setup, where the jet tends to be unipolar. This difference arises primarily from the geometry of the global magnetic field. In the disk-only case, the magnetic field structure typically facilitates the opening of a jet-launching cavity in only one hemisphere, while the other hemisphere is more likely to be choked by the disk wind. However, when a rotating stellar magnetosphere is included, the toroidal magnetic field reverses signs in both hemispheres, enabling the formation of polar cavities on both sides of the midplane. Consequently, jets driven by the

magnetosphere-disk interaction are more likely to be bipolar and symmetric.

ACKNOWLEDGMENTS

YT acknowledges support from the interdisciplinary fellowship at UVA. CYH acknowledges support from an ALMA Student Observing Support (SOS) from NRAO. We acknowledge computing resources from UVA research computing (RIVANNA), NASA High-Performance Computing, and NSF’s ACCESS computing allocation AST200032 and PHY250098. ZYL, YT, and CYH are supported in part by NASA 80NSSC20K0533, NSF AST-2307199, JWST-GO-02104.002-A, and the Virginia Institute of Theoretical Astronomy (VITA). Z.Z. acknowledges support from NSF award 2408207, 2429732 and NASA grant 80NSSC24K1285.

AUTHOR CONTRIBUTIONS

YT led the modeling, analysis, interpretation, and writing of the paper. ZYL and Z.Z. contributed to the analysis and interpretation, and oversaw the project’s progress. HX and CYH contributed to the interpretation.

REFERENCES

- Anderson, J. M., Li, Z.-Y., Krasnopolsky, R., & Blandford, R. D. 2005, *ApJ*, 630, 945, doi: [10.1086/432040](https://doi.org/10.1086/432040)
- Anderson, J. M., Li, Z.-Y., Krasnopolsky, R., & Blandford, R. D. 2006, *ApJL*, 653, L33, doi: [10.1086/510307](https://doi.org/10.1086/510307)
- André, P., Di Francesco, J., Ward-Thompson, D., et al. 2014, in *Protostars and Planets VI*, ed. H. Beuther, R. S. Klessen, C. P. Dullemond, & T. Henning, 27–51, doi: [10.2458/azu_uapress.9780816531240-ch002](https://doi.org/10.2458/azu_uapress.9780816531240-ch002)
- Arons, J., & Lea, S. M. 1976, *ApJ*, 207, 914, doi: [10.1086/154562](https://doi.org/10.1086/154562)
- Assani, K. D., Harsono, D., Ramsey, J. P., et al. 2024, *A&A*, 688, A26, doi: [10.1051/0004-6361/202449745](https://doi.org/10.1051/0004-6361/202449745)
- Bai, X.-N., & Stone, J. M. 2013, *ApJ*, 769, 76, doi: [10.1088/0004-637X/769/1/76](https://doi.org/10.1088/0004-637X/769/1/76)
- Bardou, A., & Heyvaerts, J. 1996, *A&A*, 307, 1009
- Béthune, W., Lesur, G., & Ferreira, J. 2017, *A&A*, 600, A75, doi: [10.1051/0004-6361/201630056](https://doi.org/10.1051/0004-6361/201630056)
- Bjerkeli, P., van der Wiel, M. H. D., Harsono, D., Ramsey, J. P., & Jørgensen, J. K. 2016, *Nature*, 540, 406, doi: [10.1038/nature20600](https://doi.org/10.1038/nature20600)
- Blandford, R. D., & Payne, D. G. 1982, *MNRAS*, 199, 883, doi: [10.1093/mnras/199.4.883](https://doi.org/10.1093/mnras/199.4.883)
- Blinova, A. A., Romanova, M. M., & Lovelace, R. V. E. 2016, *Monthly Notices of the Royal Astronomical Society*, 459, 2354, doi: [10.1093/mnras/stw786](https://doi.org/10.1093/mnras/stw786)
- Cacciapuoti, L., Testi, L., Podio, L., et al. 2024, *The Astrophysical Journal*, 961, 90, doi: [10.3847/1538-4357/ad0f17](https://doi.org/10.3847/1538-4357/ad0f17)
- Cai, M. J., Shang, H., Lin, H.-H., & Shu, F. H. 2008, *ApJ*, 672, 489, doi: [10.1086/523788](https://doi.org/10.1086/523788)
- Casse, F., & Keppens, R. 2002, *ApJ*, 581, 988, doi: [10.1086/344340](https://doi.org/10.1086/344340)
- Codella, C., Cabrit, S., Gueth, F., et al. 2014, *A&A*, 568, L5, doi: [10.1051/0004-6361/201424103](https://doi.org/10.1051/0004-6361/201424103)
- de Valon, A., Dougados, C., Cabrit, S., et al. 2020, *A&A*, 634, L12, doi: [10.1051/0004-6361/201936950](https://doi.org/10.1051/0004-6361/201936950)

- Delabrosse, V., Dougados, C., Cabrit, S., et al. 2024, *A&A*, 688, A173, doi: [10.1051/0004-6361/202449176](https://doi.org/10.1051/0004-6361/202449176)
- Desch, S. J., Morris, M. A., Connolly, H. C., & Boss, A. P. 2010, *The Astrophysical Journal*, 725, 692, doi: [10.1088/0004-637X/725/1/692](https://doi.org/10.1088/0004-637X/725/1/692)
- Fendt, C., & Elstner, D. 2000, *A&A*, 363, 208, doi: [10.48550/arXiv.astro-ph/0010607](https://doi.org/10.48550/arXiv.astro-ph/0010607)
- Fendt, C., & Sheikhezami, S. 2013, *The Astrophysical Journal*, 774, 12, doi: [10.1088/0004-637X/774/1/12](https://doi.org/10.1088/0004-637X/774/1/12)
- Fendt, C., Vaidya, B., Porth, O., & Nezami, S. S. 2011, in *IAU Symposium*, Vol. 275, *Jets at All Scales*, ed. G. E. Romero, R. A. Sunyaev, & T. Belloni, 383–391, doi: [10.1017/S1743921310016443](https://doi.org/10.1017/S1743921310016443)
- Galametz, M., Maury, A., Girart, J. M., et al. 2020, *A&A*, 644, A47, doi: [10.1051/0004-6361/202038854](https://doi.org/10.1051/0004-6361/202038854)
- Goodson, A. P., & Winglee, R. M. 1999, *ApJ*, 524, 159, doi: [10.1086/307780](https://doi.org/10.1086/307780)
- Guan, X., Li, H., & Li, S. 2014, *ApJ*, 781, 48, doi: [10.1088/0004-637X/781/1/48](https://doi.org/10.1088/0004-637X/781/1/48)
- Guszejnov, D., Grudić, M. Y., Hopkins, P. F., Offner, S. S. R., & Faucher-Giguère, C.-A. 2021, *MNRAS*, 502, 3646, doi: [10.1093/mnras/stab278](https://doi.org/10.1093/mnras/stab278)
- Hsieh, C.-H., Arce, H. G., Li, Z.-Y., et al. 2023, *The Astrophysical Journal*, 947, 25, doi: [10.3847/1538-4357/acba13](https://doi.org/10.3847/1538-4357/acba13)
- Hsu, S.-Y., Lee, C.-F., Liu, S.-Y., et al. 2024, *ApJ*, 976, 29, doi: [10.3847/1538-4357/ad7e25](https://doi.org/10.3847/1538-4357/ad7e25)
- Huarte-Espinosa, M., Frank, A., Blackman, E. G., et al. 2012, *ApJ*, 757, 66, doi: [10.1088/0004-637X/757/1/66](https://doi.org/10.1088/0004-637X/757/1/66)
- Jacquemin-Ide, J., Lesur, G., & Ferreira, J. 2021, *A&A*, 647, A192, doi: [10.1051/0004-6361/202039322](https://doi.org/10.1051/0004-6361/202039322)
- Jannaud, T., Zanni, C., & Ferreira, J. 2023, *A&A*, 669, A159, doi: [10.1051/0004-6361/202244311](https://doi.org/10.1051/0004-6361/202244311)
- Kato, S. X., Kudoh, T., & Shibata, K. 2002, *ApJ*, 565, 1035, doi: [10.1086/324776](https://doi.org/10.1086/324776)
- Kato, Y., Mineshige, S., & Shibata, K. 2004, *ApJ*, 605, 307, doi: [10.1086/381234](https://doi.org/10.1086/381234)
- Krasnopolsky, R., Li, Z.-Y., & Blandford, R. 1999, *ApJ*, 526, 631, doi: [10.1086/308023](https://doi.org/10.1086/308023)
- Krasnopolsky, R., Li, Z.-Y., & Blandford, R. D. 2003, *ApJ*, 595, 631, doi: [10.1086/377494](https://doi.org/10.1086/377494)
- Kuwabara, T., Shibata, K., Kudoh, T., & Matsumoto, R. 2000, *PASJ*, 52, 1109, doi: [10.1093/pasj/52.6.1109](https://doi.org/10.1093/pasj/52.6.1109)
- Lai, D. 2014, in *European Physical Journal Web of Conferences*, Vol. 64, *European Physical Journal Web of Conferences*, 01001, doi: [10.1051/epjconf/20136401001](https://doi.org/10.1051/epjconf/20136401001)
- Lankhaar, B., Vlemmings, W., & Bjerkeli, P. 2022, *A&A*, 657, A106, doi: [10.1051/0004-6361/202141285](https://doi.org/10.1051/0004-6361/202141285)
- Lee, C.-F., Tabone, B., Cabrit, S., et al. 2021, *ApJL*, 907, L41, doi: [10.3847/2041-8213/abda38](https://doi.org/10.3847/2041-8213/abda38)
- Lii, P. S., Romanova, M. M., Ustyugova, G. V., Koldoba, A. V., & Lovelace, R. V. E. 2014, *Monthly Notices of the Royal Astronomical Society*, 441, 86, doi: [10.1093/mnras/stu495](https://doi.org/10.1093/mnras/stu495)
- López-Vázquez, J. A., Lee, C.-F., Shang, H., et al. 2024, *ApJ*, 977, 126, doi: [10.3847/1538-4357/ad8eb4](https://doi.org/10.3847/1538-4357/ad8eb4)
- Lovelace, R. V. E., Li, H., Ustyugova, G. V., Romanova, M. M., & Colgate, S. A. 2001, in *American Institute of Physics Conference Series*, Vol. 586, *20th Texas Symposium on relativistic astrophysics*, ed. J. C. Wheeler & H. Martel (AIP), 426–432, doi: [10.1063/1.1419587](https://doi.org/10.1063/1.1419587)
- Lovelace, R. V. E., & Romanova, M. M. 2009, arXiv e-prints, arXiv:0901.4753, doi: [10.48550/arXiv.0901.4753](https://doi.org/10.48550/arXiv.0901.4753)
- Lovelace, R. V. E., Romanova, M. M., & Lii, P. 2013, arXiv e-prints, arXiv:1306.1160, doi: [10.48550/arXiv.1306.1160](https://doi.org/10.48550/arXiv.1306.1160)
- Lovelace, R. V. E., Romanova, M. M., Lii, P., & Dyda, S. 2014, *Computational Astrophysics and Cosmology*, 1, 3, doi: [10.1186/s40668-014-0003-5](https://doi.org/10.1186/s40668-014-0003-5)
- Lynden-Bell, D. 1996, *MNRAS*, 279, 389, doi: [10.1093/mnras/279.2.389](https://doi.org/10.1093/mnras/279.2.389)
- Lynden-Bell, D. 2003, *Monthly Notices of the Royal Astronomical Society*, 341, 1360, doi: [10.1046/j.1365-8711.2003.06506.x](https://doi.org/10.1046/j.1365-8711.2003.06506.x)
- Matt, S., Goodson, A. P., Winglee, R. M., & Böhm, K.-H. 2002, *ApJ*, 574, 232, doi: [10.1086/340896](https://doi.org/10.1086/340896)
- Mattia, G., & Fendt, C. 2020a, *The Astrophysical Journal*, 900, 59, doi: [10.3847/1538-4357/aba9d7](https://doi.org/10.3847/1538-4357/aba9d7)
- Mattia, G., & Fendt, C. 2020b, *The Astrophysical Journal*, 900, 60, doi: [10.3847/1538-4357/aba9d6](https://doi.org/10.3847/1538-4357/aba9d6)
- Miller, K. A., & Stone, J. M. 1997, *ApJ*, 489, 890, doi: [10.1086/304825](https://doi.org/10.1086/304825)
- Mishra, B., Begelman, M. C., Armitage, P. J., & Simon, J. B. 2020, *MNRAS*, 492, 1855, doi: [10.1093/mnras/stz3572](https://doi.org/10.1093/mnras/stz3572)
- Moll, R., Spruit, H. C., & Obergaulinger, M. 2008, *A&A*, 492, 621, doi: [10.1051/0004-6361:200810523](https://doi.org/10.1051/0004-6361:200810523)
- Morbidelli, A., Marocchi, Y., Ali Ahmad, A., et al. 2024, *A&A*, 691, A147, doi: [10.1051/0004-6361/202451388](https://doi.org/10.1051/0004-6361/202451388)
- Nakamura, M., Li, H., & Li, S. 2007, *ApJ*, 656, 721, doi: [10.1086/510361](https://doi.org/10.1086/510361)
- Ohashi, S., Muto, T., Tsukamoto, Y., et al. 2025, *Nature Astronomy*, doi: [10.1038/s41550-024-02454-x](https://doi.org/10.1038/s41550-024-02454-x)
- Oishi, J. S., Vasil, G. M., Baxter, M., et al. 2020, *Proceedings of the Royal Society of London Series A*, 476, 20190622, doi: [10.1098/rspa.2019.0622](https://doi.org/10.1098/rspa.2019.0622)
- Pascucci, I., Cabrit, S., Edwards, S., et al. 2023, in *Astronomical Society of the Pacific Conference Series*, Vol. 534, *Protostars and Planets VII*, ed. S. Inutsuka, Y. Aikawa, T. Muto, K. Tomida, & M. Tamura, 567, doi: [10.48550/arXiv.2203.10068](https://doi.org/10.48550/arXiv.2203.10068)

- Podio, L., Codella, C., Gueth, F., et al. 2015, *A&A*, 581, A85, doi: [10.1051/0004-6361/201525778](https://doi.org/10.1051/0004-6361/201525778)
- Pudritz, R. E., & Norman, C. A. 1983, *ApJ*, 274, 677, doi: [10.1086/161481](https://doi.org/10.1086/161481)
- Ramsey, J. P., & Clarke, D. A. 2019, *MNRAS*, 484, 2364, doi: [10.1093/mnras/stz116](https://doi.org/10.1093/mnras/stz116)
- Ray, T., & Ferreira, J. 2021, *New Astronomy Reviews*, 93, 101615, doi: <https://doi.org/10.1016/j.newar.2021.101615>
- Romanova, M. M., Espaillat, C. C., Wendeborn, J., et al. 2025, *MNRAS*, 538, 480, doi: [10.1093/mnras/staf148](https://doi.org/10.1093/mnras/staf148)
- Romanova, M. M., Koldoba, A. V., Ustyugova, G. V., et al. 2021, *MNRAS*, 506, 372, doi: [10.1093/mnras/stab1724](https://doi.org/10.1093/mnras/stab1724)
- Romanova, M. M., Kulkarni, A. K., & Lovelace, R. V. E. 2008, *The Astrophysical Journal*, 673, L171, doi: [10.1086/527298](https://doi.org/10.1086/527298)
- Romanova, M. M., Ustyugova, G. V., Koldoba, A. V., & Lovelace, R. V. E. 2005, *ApJL*, 635, L165, doi: [10.1086/499560](https://doi.org/10.1086/499560)
- Romanova, M. M., Ustyugova, G. V., Koldoba, A. V., & Lovelace, R. V. E. 2009, *MNRAS*, 399, 1802, doi: [10.1111/j.1365-2966.2009.15413.x](https://doi.org/10.1111/j.1365-2966.2009.15413.x)
- Romanova, M. M., Ustyugova, G. V., Koldoba, A. V., & Lovelace, R. V. E. 2012, *MNRAS*, 421, 63, doi: [10.1111/j.1365-2966.2011.20055.x](https://doi.org/10.1111/j.1365-2966.2011.20055.x)
- Shang, H., Glassgold, A. E., Shu, F. H., & Lizano, S. 2002, *ApJ*, 564, 853, doi: [10.1086/324197](https://doi.org/10.1086/324197)
- Shibata, K., & Uchida, Y. 1986, *PASJ*, 38, 631
- Shu, F., Najita, J., Ostriker, E., et al. 1994, *ApJ*, 429, 781, doi: [10.1086/174363](https://doi.org/10.1086/174363)
- Shu, F. H., Najita, J., Ostriker, E. C., & Shang, H. 1995, *ApJL*, 455, L155, doi: [10.1086/309838](https://doi.org/10.1086/309838)
- Shu, F. H., Najita, J. R., Shang, H., & Li, Z. Y. 2000, in *Protostars and Planets IV*, ed. V. Mannings, A. P. Boss, & S. S. Russell, 789–814
- Spruit, H. C., Stehle, R., & Papaloizou, J. C. B. 1995, *Monthly Notices of the Royal Astronomical Society*, 275, 1223, doi: [10.1093/mnras/275.4.1223](https://doi.org/10.1093/mnras/275.4.1223)
- Stepanovs, D., & Fendt, C. 2016, *The Astrophysical Journal*, 825, 14, doi: [10.3847/0004-637X/825/1/14](https://doi.org/10.3847/0004-637X/825/1/14)
- Stone, J. M., Tomida, K., White, C. J., & Felker, K. G. 2020, *ApJS*, 249, 4, doi: [10.3847/1538-4365/ab929b](https://doi.org/10.3847/1538-4365/ab929b)
- Tabone, B., Cabrit, S., Bianchi, E., et al. 2017, *A&A*, 607, L6, doi: [10.1051/0004-6361/201731691](https://doi.org/10.1051/0004-6361/201731691)
- Takaishi, D., Tsukamoto, Y., Kido, M., et al. 2024, *ApJ*, 963, 20, doi: [10.3847/1538-4357/ad187a](https://doi.org/10.3847/1538-4357/ad187a)
- Takasao, S., Hosokawa, T., Tomida, K., & Iwasaki, K. 2025, arXiv e-prints, arXiv:2503.15350. <https://arxiv.org/abs/2503.15350>
- Takasao, S., Tomida, K., Iwasaki, K., & Suzuki, T. K. 2019, *ApJL*, 878, L10, doi: [10.3847/2041-8213/ab22bb](https://doi.org/10.3847/2041-8213/ab22bb)
- Takasao, S., Tomida, K., Iwasaki, K., & Suzuki, T. K. 2022, *The Astrophysical Journal*, 941, 73, doi: [10.3847/1538-4357/ac9eb1](https://doi.org/10.3847/1538-4357/ac9eb1)
- Tsukamoto, Y., Machida, M. N., & Inutsuka, S.-i. 2021, *ApJL*, 920, L35, doi: [10.3847/2041-8213/ac2b2f](https://doi.org/10.3847/2041-8213/ac2b2f)
- Tu, Y., Li, Z.-Y., Lam, K. H., Tomida, K., & Hsu, C.-Y. 2024, *MNRAS*, 527, 10131, doi: [10.1093/mnras/stad3843](https://doi.org/10.1093/mnras/stad3843)
- Tu, Y., Li, Z.-Y., Zhu, Z., Hsu, C.-Y., & Hu, X. 2025a, arXiv e-prints, arXiv:2502.20495, doi: [10.48550/arXiv.2502.20495](https://doi.org/10.48550/arXiv.2502.20495)
- Tu, Y., Li, Z.-Y., Zhu, Z., Hu, X., & Hsu, C.-Y. 2025b, *ApJ*, 978, 84, doi: [10.3847/1538-4357/ad927b](https://doi.org/10.3847/1538-4357/ad927b)
- Tzeferacos, P., Ferrari, A., Mignone, A., et al. 2009, *MNRAS*, 400, 820, doi: [10.1111/j.1365-2966.2009.15502.x](https://doi.org/10.1111/j.1365-2966.2009.15502.x)
- Ustyugova, G. V., Koldoba, A. V., Romanova, M. M., Chechetkin, V. M., & Lovelace, R. V. E. 1999, *ApJ*, 516, 221, doi: [10.1086/307093](https://doi.org/10.1086/307093)
- Uzdensky, D. A. 2002, *ApJ*, 572, 432, doi: [10.1086/340308](https://doi.org/10.1086/340308)
- Čemeljić, M., Shang, H., & Chiang, T. Y. 2013, *ApJ*, 768, 5, doi: [10.1088/0004-637X/768/1/5](https://doi.org/10.1088/0004-637X/768/1/5)
- Vlemmings, W. H. T., Lankhaar, B., Cazzoletti, P., et al. 2019, *A&A*, 624, L7, doi: [10.1051/0004-6361/201935459](https://doi.org/10.1051/0004-6361/201935459)
- Whelan, E. T., Keppler, M., Turner, N. J., et al. 2024, *ApJ*, 974, 293, doi: [10.3847/1538-4357/ad6c4e](https://doi.org/10.3847/1538-4357/ad6c4e)
- Wurster, J., & Li, Z.-Y. 2018, *Frontiers in Astronomy and Space Sciences*, 5, 39, doi: [10.3389/fspas.2018.00039](https://doi.org/10.3389/fspas.2018.00039)
- Yen, H.-W., Williams, J. P., Sai, J., et al. 2024, *ApJ*, 969, 125, doi: [10.3847/1538-4357/ad4c6b](https://doi.org/10.3847/1538-4357/ad4c6b)
- Zanni, C., & Ferreira, J. 2013, *A&A*, 550, A99, doi: [10.1051/0004-6361/201220168](https://doi.org/10.1051/0004-6361/201220168)
- Zhu, Z. 2025, *Monthly Notices of the Royal Astronomical Society*, 537, 3701, doi: [10.1093/mnras/staf250](https://doi.org/10.1093/mnras/staf250)
- Zhu, Z., & Stone, J. M. 2018, *ApJ*, 857, 34, doi: [10.3847/1538-4357/aaafc9](https://doi.org/10.3847/1538-4357/aaafc9)
- Zhu, Z., Stone, J. M., & Calvet, N. 2024, *MNRAS*, 528, 2883, doi: [10.1093/mnras/stad3712](https://doi.org/10.1093/mnras/stad3712)